

COSMOGLOBE DR2. VI. Disentangling hot and cold thermal dust emission with Planck HFI

R. M. Sullivan^{1*}, E. Gjerløw¹, R. Aurvik¹, A. Basyrov¹, L. A. Bianchi¹, A. Bonato², M. Brilenkov¹, H. K. Eriksen¹, U. Fuskeland¹, M. Galloway¹, K. A. Glasscock¹, L. T. Hergt³, D. Herman¹, J. G. S. Lunde¹, A. I. Silva Martins¹, M. San¹, D. Sponseller⁴, N.-O. Stutzer¹, H. Thommesen¹, V. Vikenes¹, D. J. Watts¹, I. K. Wehus¹, and L. Zapelli^{2,5,6}

¹ Institute of Theoretical Astrophysics, University of Oslo, Blindern, Oslo, Norway

² Dipartimento di Fisica, Università degli Studi di Milano, Via Celoria, 16, Milano, Italy

³ Department of Physics and Astronomy, University of British Columbia, 6224 Agricultural Road, Vancouver BC, V6T1Z1, Canada

⁴ Department of Space, Earth and Environment, Chalmers University of Technology, Gothenburg, Sweden

⁵ Università di Trento, Università degli Studi di Milano, CUP E66E23000110001

⁶ INFN sezione di Milano, 20133 Milano, Italy

January 12, 2026

ABSTRACT

We present a four-component high-resolution model of thermal dust emission for microwave and infrared frequencies derived from *Planck* HFI, WHAM and *Gaia*. This model is inspired by a joint low-resolution template-based analysis of *Planck* HFI and *COBE*-DIRBE data presented in Gjerløw et al. (2026a), and the resulting high-resolution model forms the basis for the thermal dust model employed in the COSMOGLOBE DR2 reanalysis of *COBE*-DIRBE. The four dust components correspond to different semi-independent physical effects, referred to as “cold dust”, “hot dust”, “nearby dust”, and “H α correlated dust”. The H α dust is a dust extinction component, and has a negative amplitude in the *Planck* HFI bands. The spatial distributions of the nearby dust and H α dust components are defined by a *Gaia* 3D extinction model (Edenhofer et al. 2024) and the Wisconsin H α mapper (WHAM; Haffner et al. 2003, 2016), respectively, while the hot and cold dust components are fit freely pixel-by-pixel to the *Planck* HFI data. We use a parameter grid search (for global parameters) coupled to a Bayesian Gibbs sampler (for per-pixel parameters) to fit this model to *Planck* HFI data. The fiducial MBB temperature for the hot and cold dust components are $T_h = 30 \pm 3$ K and $T_c = 11 \pm 1$ K, and the corresponding fiducial spectral indices are $\beta_h \geq 1.75$ and $\beta_c = 1.85 \pm 0.10$, respectively. In agreement with the low-resolution template fit analysis of Gjerløw et al. (2026a), we find that the hot dust component is strongly correlated with the FIRAS C II map, while the cold dust component is strongly correlated with the HI4PI H I. Despite its fewer degrees of freedom per pixel compared to the *Planck* 2018 legacy dust model, we find that this new model performs competitively in terms of overall residuals, capturing between 98.5 and 99.9 % of the full-sky dust rms for all channels between 100 and 857 GHz. When fitting a spatially varying 3-parameter MBB model to the new four-component dust model with isotropic SEDs, we find similar spatial distributions of T and β to those of the official *Planck* analysis. We conclude that this new model represents both a statistically more efficient summary of thermal dust in the microwave and far-infrared regimes, as well as a physically more realistic decomposition of the sky, compared to the traditional 3-parameter MBB model, due to its strong correlations with well-defined C II and H I line emission tracers. Finally, we expect that the novel templates of hot and cold dust emission presented in this paper may form a key component in future temperature and polarization measurements for projects such as Simons Observatory and *LiteBIRD*, where high-precision measurements of the dust will be critical for constraining *B*-mode CMB polarization.

Key words. ISM: general - Cosmology: observations, diffuse radiation - Galaxy: general

1. Introduction

Observing the Universe through a screen of foregrounds offers opportunities for both discovery and frustration (Planck Collaboration 2018; Planck Collaboration IV 2020; Ade et al. 2014). The foregrounds ultimately complicate our understanding of the backgrounds, and when poorly understood, lead to increased uncertainties or even misinterpretations. A better understanding of the foregrounds allows us to uncover the physics permeating matter on all scales, from within our solar system (e.g., Kellogg et al. 1998), to the Milky Way (e.g., Planck Collaboration X 2016), to distant galaxies (e.g., Planck Collaboration Int. XXV 2015; Planck Collaboration Int. XXVI 2015; Planck Collaboration X 2011), while simultaneously allowing us to better ob-

serve the far away signals of the Cosmic Microwave Background (CMB; Penzias & Wilson 1965) and the Cosmic Infrared Background (CIB; Partridge & Peebles 1967), among others. Of particular interest to this paper and the cosmology community at large is the composition of thermal dust (e.g., Planck Collaboration XI 2014; Hensley & Draine 2023). Thermal dust represents a significant noise contribution to future measurements of primordial polarization *B*-modes (BICEP2 Collaboration 2018), predicted to have been generated by gravitational waves during inflation () which is the primary goal of several ongoing or upcoming CMB experiments (LiteBIRD Collaboration et al. 2023; Ade et al. 2019).

Aside from the aforementioned dust, the Milky Way contains gas (generating emission lines such as singly ionized carbon (C II), hydrogen emission lines such as H α , neutral hydrogen (H I), carbon monoxide (CO) and many more), stars, spin-

* Corresponding author: R. M. Sullivan; raelyn.sullivan@astro.uio.no

ning dust, ions and electrons (interacting with magnetic fields to produce synchrotron and free-free radiation) and dark matter (only thus far interacting gravitationally). Each of these foregrounds trace relevant regions of the Milky Way and the interstellar medium (ISM). Since dust and gas live side-by-side, it is natural that one may trace the other, and indeed it is known that the neutral hydrogen signature (as observed by, e.g., HI4PI, HI4PI Collaboration et al. 2016) and CO (Dame et al. 2001) trace cold dust. Another observable we can use is the reddening or extinction measurements of starlight, which occurs when their light passes through dust regions (e.g., Lenz et al. 2017; Lallement et al. 2022; Edenhofer et al. 2024). Finally, as recently shown by Gjerløw et al. (2026a), the C II emission lines, as measured by COBE-FIRAS (Mather et al. 1994), trace hot dust regions. Before Gjerløw et al. (2026a) it was not known to us that C II could be used directly as a high-precision dust tracer; however, as it is expected to be present in hot regions of the Milky Way, it is not unexpected that this acts as a tracer for the hot dust.¹

The dust in the Milky Way will act to absorb radiation at frequencies close to its particle size and re-emit as an imperfect blackbody. Historically, this has been modeled with a modified blackbody spectrum (MBB) characterized by a temperature, T , and a ‘tilt’ to the spectrum, called the spectral index and denoted by β . These, along with an amplitude (a), define how much radiation at a particular frequency, ν , is produced (see Hensley & Draine (2023) for a recent review of dust and the interstellar medium). During the *Planck* analysis the dust in the Milky Way was often modelled with a single modified blackbody fit for each pixel, or direction, in the sky. However, it is known that there are different dust populations (Finkbeiner et al. 1999), and with enough data it should be possible to make distinct templates modelling each independently. A significant challenge that *Planck* faced in their analysis was that there was insufficient data to distinguish these populations; in particular, there is a clear degeneracy between the dust temperature and the dust spectral index maps (Juvela & Ysard 2012; Planck Collaboration X 2016).

In the current paper, we revisit the model introduced by Gjerløw et al. (2026a). In that paper, the authors found that thermal dust emission in the *Planck* HFI and COBE-DIRBE data on large angular scales could be very well described by a sum of five external dust templates, namely 1) COBE-FIRAS C II; 2) HI4PI (HI4PI Collaboration et al. 2016); 3) *Gaia* extinction (Edenhofer et al. 2024); 4) WHAM H α (Haffner et al. 2003, 2016); and 5) CO J=1 – 0 (Dame et al. 2001). They furthermore noted that the C II map template associated with a higher temperature than the HI4PI and CO templates; that the nearby *Gaia* extinction template corresponded to an intermediate temperature; and that the H α template was observed in absorption (i.e., having a negative template amplitude). The main goal of the current paper is to establish a corresponding multi-component model for *Planck* HFI at full angular resolution. Since the FIRAS C II map has a very low angular resolution of 7° FWHM, this means that the morphology of the hotter dust component has to be derived directly from the *Planck* data, rather than traced by an already existing template. Furthermore, the HI4PI and Dame et al. templates also have issues that prevent their direct use as a template (e.g., lower resolution and/or incomplete sky coverage). The key operational step in the current analysis is therefore to establish separate maps of cold and hot dust directly from the *Planck* HFI data them-

selves. Since we do not use a template for the hot and cold dust, this also acts as a confirmation of the effects seen in Gjerløw et al. (2026a), as the *Planck* data set is independent of the DIRBE data set, both in terms of the frequencies observed and the telescope. Finding a cold and hot dust component tightly tracing the H I and C II gas acts as a strong confirmation of the results previously shown.

Following Gjerløw et al. (2026a), we adopt the maps produced by Edenhofer et al. (2024) with *Gaia* data (Gaia Collaboration et al. 2016) to trace nearby dust in the Milky Way, and the H α map produced by the Wisconsin H- α mapper (WHAM) (Haffner et al. 2003, 2016) to trace a sub-dominant level of dust absorption. These two data sets are used as templates, fixing the relative amplitudes between pixels, but allowing the overall amplitudes of the maps, as well as the temperature and spectral indices, to vary globally. We introduce two additional dust components, here called the hot and the cold dust, which have freely varying amplitudes per pixel, but a global temperature and spectral index. Compared to the previous *Planck* analysis, which had three free parameters per pixel, we instead have ten global parameters, with only two free parameters per pixel, the hot and cold dust amplitudes. At high resolutions this represents a significant reduction in the number of model parameters, and has the additional advantage of producing clear correlations between the cold dust and the HI4PI maps (a known cold dust tracer), and the hot dust and C II.

This paper is one of seven companion papers from the CosMOGLOBE data release 2 (DR2; Watts et al. 2024a) reanalyzing the COBE-DIRBE data (Hauser et al. 1998). Of particular interest for this release is new constraints on the spectrum of the CIB (Watts et al. 2024b), and better constraints on all foregrounds ranging from the microwave to the infrared, including zodiacal light (San et al. 2024) and stars (Galloway et al. 2026). In a companion dust paper, by Gjerløw et al. (2026a), we perform a linear regression analysis of *Planck* HFI 353–857 GHz and DIRBE 3.5–100 μm data to a five template dust model with minimal assumptions. That analysis clearly demonstrates that there are distinct dust populations that can be modelled independently with sufficient data sets at a wide range of frequencies, and revealed the new dust tracer, the C II line emission, tracing hot dust. Building off of that work, in the current paper we perform a Bayesian analysis of the *Planck* HFI data, deriving high-resolution templates of H I and C II correlated dust components, as well as the H α and nearby dust template fits. Finally, in Gjerløw et al. (2026b) this new dust model is applied to the COBE-DIRBE data.

The rest of the paper is organized as follows. In Sect. 2 we discuss the data sets we use for this analysis. We next discuss the sky and data model in Sect. 3. In Sect. 4 we discuss our methodology, primarily the Gibbs sampling and grid search tests, along with the optimization strategy used for the grid search. In Sect. 5 we present the best fit results for our new thermal dust model. In Sect. 6 we discuss the goodness of fit of the model, and in Sect. 7 the correlations with external line emission maps. In Sect. 8 we compare to the previous *Planck* results and show the MBB fit to the multi-component dust model. Finally, in Sect. 9 we present our conclusions. In appendix A, appendix B, appendix C, appendix D and appendix E we include supplementary details regarding the data preprocessing, dust templates, residuals, the grid search, and the dust characterization for clarity.

2. Data

Building on the work of Gjerløw et al. (2026a), this analysis uses the *Planck* PR4 data (Sect. 2.1), several FIRAS maps (Sect. 2.2),

¹ It has also been hypothesized that dust may be responsible for the C II deficit in luminous-FIR galaxies (Jackson et al. 2020; Díaz-Santos et al. 2017).

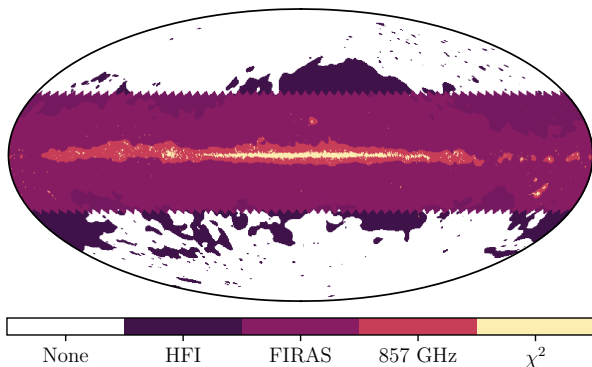


Fig. 1: All masks used for different stages of the analysis. *HFI*: Mask used during the HFI Gibbs sampling routine for the monopoles, dipoles and χ^2 evaluation. *FIRAS*: Mask used during the FIRAS Gibbs sampling routine for the monopoles, dipoles and χ^2 evaluation. *857 GHz*: Mask used during the 857 GHz gain Gibbs sampling routine. χ^2 : Mask used to compare the χ^2 in the grid search.

152 and additional ancillary data (Sect. 2.3) to constrain a new high
153 resolution four component dust model. We discuss our masks in
154 Sect. 2.4.

155 2.1. Planck HFI

156 The *Planck* PR4 (also known as NPIPE) maps are the final
157 *Planck* data release, improving on previous data releases by
158 jointly analyzing the low-frequency instrument (LFI) and the
159 high-frequency instrument (HFI) data in a single pipeline, in ad-
160 dition to numerous other improvements (for details see *Planck*
161 *Collaboration Int. LVII* (2020)). For this analysis we use the
162 single-horn HFI maps, chosen because HFI offers strong con-
163 straining power on the dust and the single-horn maps are able to
164 better control the gain fluctuations and model components such
165 as the CO-emission.² Specifically we use the 100–{1-4}, 143–
166 {1-7}, 217–{1-8}, 353–{1-8}, 545–{1,2,4} and 857–{1-4}.⁴ In
167 a pre-processing step we correct all maps for the zodiacal light
168 emission, using the *Planck* PR2 zodiacal light model (*Planck*
169 *Collaboration VIII* 2016; *Planck Collaboration XIV* 2014; Maris
170 et al. 2006), and apply a correction for the CIB to the 857, 545
171 and 353 GHz maps from the GNILC CIB results *Planck Collabora-*
172 *tion Int. XLVIII* (2016). We apply a scaling correction to the
173 root-mean squared (RMS) maps, such that the tail of the map
174 power spectra match the white-noise level from the RMS maps.⁵
175 These scaling values can be found in appendix A.

176 2.2. FIRAS

177 FIRAS was a cosmology telescope, launched in 1989 as part
178 of the COBE satellite mission, with the goal of measuring the
179 blackbody spectrum of the CMB to unprecedented precision

² The 100 GHz and 143 GHz maps are at a HEALPix³ pixelization (Górski et al. 2005; Zonca et al. 2019) N_{side} of 2048, the other frequencies are at an N_{side} of 4096.

⁴ The 143-8 and 545-3 maps were never released by the *Planck* collaboration due to non-Gaussian noise in the data, known as random telegraphic signal (*Planck Collaboration VI* 2014).

⁵ The published single horn frequency RMS maps have known residual offsets from the analysis pipeline, evident when comparing the map and RMS power-spectra.

(Fixsen et al. 1997). The FIRAS maps have very low calibration
180 uncertainties, and so we use them to help calibrate the map am-
181 plitudes. The FIRAS 857, 1251, 1809, 2081, 2135 and 2802 GHz
182 maps are used for this analysis in conjunction with the HFI maps.
183

184 2.3. Ancillary data

The nearby dust relative amplitudes are fixed to the *Gaia*-based
185 dust extinction template produced by Edenhofer et al. (2024),
186 which covers distances up to 1.25 kpc. This primarily uses *Gaia*
187 distances and extinction estimates to build a 3D map of the
188 nearby dust from Zhang et al. (2023) and *Gaia* (Zucker et al.
189 2019; Montegriffo et al. 2023), which also leverages the two Mi-
190 cron All Sky Survey (2MASS, Skrutskie et al. (2006)), the Wide-
191 field Infrared Survey Explorer (WISE and unWISE; Cutri et al.
192 (2013); Wright et al. (2010)), the Large sky Area Multi-Object
193 fibre Spectroscopic Telescope (LAMOST; Xiang & Rix (2023);
194 Xiang et al. (2022); Wang et al. (2022a,b)). We use the total in-
195 tegrated dust map as our model in this analysis. Additionally,
196 we use the Wisconsin H- α Mapper (WHAM) data (Haffner et al.
197 2003, 2016) as a template for the H- α correlated dust and the re-
198 sults from (Gjerłøw et al. 2026a) as the fiducial values for the H- α
199 MBB, since we find that it is poorly constrained by the *Planck*
200 bands (see Sect. 5). As with DIRBE, the H- α dust is a small ex-
201 tinction component in the *Planck* bands. When considering our
202 summary statistics in Sect. 7 we compare the new dust templates
203 with the 157.7 μm C II line emission as measured by the FIRAS
204 C II map, available on the LAMBDA⁶ website, and to the HI4PI
205 data (HI4PI Collaboration et al. 2016).

207 2.4. Masks

When computing the χ^2 for the grid search (see Sect. 4.2) we
208 apply a mask to remove the extreme outliers in the χ^2 map, as
209 can be seen in yellow in Fig. 1, this has an f_{sky} of 99% (masking
210 only 1% of the sky). During the Gibbs sampling (see Sect. 4.1),
211 we apply a 30 degree galactic plane mask to the FIRAS maps
212 when computing monopole and dipole estimates (representing
213 an f_{sky} of 50%), and a large galactic cut (of areas with the largest
214 foregrounds) to the HFI maps with an f_{sky} of 48%, as can be seen
215 in dark and light purple in Fig. 1. When estimating the gain for
216 the 857 GHz maps we employ a small mask of f_{sky} of 95%, as
217 seen in orange in Fig. 1. The component estimation (as discussed
218 in Sect. 3) was done using the full sky.

220 3. Data model

221 The data model for this analysis can be written as

$$\begin{aligned} \mathbf{d} = & \mathbf{G} \left[\mathbf{B} \sum_s \mathbf{M}_s \mathbf{a}_s \right] + \mathbf{n} \\ & \equiv \mathbf{s} + \mathbf{n}, \end{aligned} \quad (1)$$

where \mathbf{G} is the instrumental gain matrix for each detector, \mathbf{B} the
222 instrumental beam convolution, $\mathbf{M}_s \mathbf{a}_s$ is the foregrounds mixing
223 matrix which extrapolates the sky component s to the given fre-
224 quency (including bandpass and the spectral shape of the partic-
225 ular component) and amplitudes \mathbf{a}_s per pixel for the various sky
226 components (s), and \mathbf{n} is the noise.

227 The *Planck* HFI bands contain several relevant sky compo-
228 nents in addition to dust, such as free-free, CO, and the CMB.
229

⁶ lambda.gsfc.nasa.gov

230 As such, the sky model used for this analysis may be written as
 231 a vector per pixel

$$\begin{aligned}
 s_\nu = & u_\nu \left[\mathbf{a}_{\text{CMB}} \gamma(\nu) \right. & (\text{CMB}) \\
 & + \mathbf{t}_{\text{ff}} \left(\frac{\nu_{0,\text{ff}}}{\nu} \right)^2 \frac{g_{\text{ff}}(\nu; T_e)}{g_{\text{ff}}(\nu_{0,\text{ff}}; T_e)} & (\text{Free-free}) \\
 & + \mathbf{a}_c \left(\frac{\nu}{\nu_c} \right)^{\beta_c+1} \left(\frac{e^{h\nu_c/k_B T_c} - 1}{e^{h\nu/k_B T_c} - 1} \right) & (\text{Cold dust}) \\
 & + \mathbf{a}_h \left(\frac{\nu}{\nu_h} \right)^{\beta_h+1} \left(\frac{e^{h\nu_h/k_B T_h} - 1}{e^{h\nu/k_B T_h} - 1} \right) & (\text{Hot dust}) \\
 & + a_{\text{near}} \mathbf{t}_{\text{near}} \left(\frac{\nu}{\nu_{\text{near}}} \right)^{\beta_{\text{near}}+1} \left(\frac{e^{h\nu_{\text{near}}/k_B T_{\text{near}}} - 1}{e^{h\nu/k_B T_{\text{near}}} - 1} \right) & (\text{Nearby dust}) \\
 & + a_{\text{H}\alpha} \mathbf{t}_{\text{H}\alpha} \left(\frac{\nu}{\nu_{\text{H}\alpha}} \right)^{\beta_{\text{H}\alpha}+1} \left(\frac{e^{h\nu_{\text{H}\alpha}/k_B T_{\text{H}\alpha}} - 1}{e^{h\nu/k_B T_{\text{H}\alpha}} - 1} \right) & (\text{H}\alpha \text{ dust}) \\
 & \left. + \mathbf{a}_{\text{co}}^{100} h_\nu^{100} + \mathbf{a}_{\text{co}}^{217} h_\nu^{217} + \mathbf{a}_{\text{co}}^{353} h_\nu^{353} \right] & (\text{CO}) \\
 & + m_\nu, & (\text{Monopole}) \\
 \end{aligned} \tag{2}$$

232 where u_ν is a unit scaling conversion factor to go from brightness
 233 temperature to thermodynamic temperature, $\gamma(\nu)$ represents the
 234 CMB fluctuation spectrum in brightness temperature (including
 235 the CMB dipole and associated effects), \mathbf{a} are the amplitudes
 236 sampled per-pixel for the CMB (\mathbf{a}_{CMB}), cold dust (\mathbf{a}_c), hot dust
 237 (\mathbf{a}_h), and the CO lines ($\mathbf{a}_{\text{co}}^{\{100,217,353\}}$). We keep the CO line-ratios
 238 ($h_\nu^{\{100,217,353\}}$) fixed to the *Planck* values [Planck Collaboration Int. LVI \(2020\)](#) for this analysis. We also keep the free-free component fixed due to the low constraining power of the HFI bands on the free-free emission. The template we use has electron temperature (T_e) of 7000 K and amplitudes (\mathbf{t}_{ff}) and Gaunt factor (g_{ff}) from the Beyond Planck analysis [BeyondPlanck Collaboration \(2023\)](#). We apply amplitude scale values, a_{near} and $a_{\text{H}\alpha}$, to the templates (\mathbf{t}_{near} based on [Edenhofer et al. \(2024\)](#) and $\mathbf{t}_{\text{H}\alpha}$ based on [Haffner et al. \(2003, 2016\)](#)) for the nearby dust (near) and H α correlated (H α) dust respectively. Finally, the monopoles (m_ν) are sampled for each frequency band. As mentioned in Sect. 2.1 we have corrected the maps for the CIB and zodiacal light, so these are not included here. We also omit synchrotron and anomalous microwave emission (AME) which are subdominant in the HFI frequency range. Note that, while in [Gjerløw et al. \(2026a\)](#) we fit a five-component dust model, of which one is the carbon monoxide correlated dust, in this case we only have the four-components. Since the true CO emission is highly correlated with the CO dust component and since we don't include the DIRBE sensitive CO channels it is effectively merged with the cold dust component.

259 4. Methods

260 Given the data model presented in Sect. 3, here we discuss the
 261 two methods used to constrain the model, Bayesian Gibbs sampling
 262 for pixel-by-pixel fit parameters (see Sect. 4.1), and a parameter grid search for the global parameters (see Sect. 4.2).

264 4.1. Bayesian analysis and Gibbs sampling

265 For the per-pixel parameters in Eqs. (1) and (2) we use a
 266 Bayesian Gibbs sampler. Gibbs sampling ([Geman & Geman](#)

Table 1: Spectral parameters for the fiducial model found in the grid search.

Component	T (K)	β	a scale
Cold dust	11 ± 1	1.85 ± 0.1	-
Hot dust	30 ± 3	≥ 1.75	-
H α dust	17.8^a	2.62^a	1^a
Nearby dust	18 ± 2	1.7 ± 0.1	$\leq 1^b$
^a <i>Hα dust is poorly constrained by the HFI data and so are set to the DIRBE fits (Gjerløw et al. 2026a).</i>			
^b <i>The amplitude scale for the fiducial value is scaled to 1 and samples in Fig. 3 are sampled around this scale.</i>			

Table 2: Gain values for 545 and 857 GHz bands. The gains for 857 GHz were sampled during the Gibbs loop, the 545 gains were fixed to input values.

Band	545-1	545-2	545-4	
Gain scale ^a	0.99145	1.00487	1.00830	
Band	857-1	857-2	857-3	857-4
Gain scale ^b	0.99362	1.10242	1.02393	1.13470

^a *The 545 GHz gains from NPIPE have an uncertainty around 0.005 percent ([Planck Collaboration Int. LVII 2020](#)).*

^b *The 857 GHz gains sampled from the grid search and in the Gibbs sampling show uncertainties at the 0.001 level.*

1984) is a Monte-Carlo sampling technique useful for very high 267 dimensional parameter spaces, such as our per-pixel amplitudes, 268 as it allows you to iteratively sample the various parameters in 269 turn instead of having to draw samples from the complete distribution. 270 Our Gibbs sampler for this case employs the algorithm 271

$$\mathbf{a}_s \leftarrow P(\mathbf{a}_s \mid \mathbf{d}, \mathbf{G}_{857}, m) \tag{3}$$

$$\mathbf{G}_{857} \leftarrow P(\mathbf{G}_{857} \mid \mathbf{d}, \mathbf{a}_s, m) \tag{4}$$

$$m \leftarrow P(m \mid \mathbf{d}, \mathbf{a}_s, \mathbf{G}_{857}), \tag{5}$$

where the arrow operator \leftarrow indicates updating the variable on 272 the left with a sample drawn from the conditional distribution 273 on the right. First, the amplitudes for all the components s (in- 274 cluding dust, CMB, and CO, as discussed in Sect. 3) are sam- 275 pled while holding the 857 GHz gains (\mathbf{G}_{857}) and monopoles 276 (m) fixed, and proceeding through the subsequent two steps be- 277 fore looping back to the first stage, obtaining samples for each 278 free parameter. We do not sample the gains for bands other 279 than the 857 GHz frequency channels, as their effects on the 280 rest of the chain were negligible. The amplitudes \mathbf{a}_s are by far 281 the most expensive step, as they represent per-pixel parameters 282 across the full sky at high resolution, whereas the gains and 283 monopoles are a single parameter per channel. For a detailed 284 discussion of the Gibbs sampling see [BeyondPlanck Collaboration \(2023\)](#); [Eriksen et al. \(2008\)](#) and references therein. This 285 approach is the foundation of the COSMOLOBE framework, based 286 on the Commander software ([Galloway et al. 2023](#)) used throughout 287 this data release. 288

290 4.2. Parameter grid search and optimization strategy

We found that the four dust components were highly correlated, 291 which meant that the Gibbs sampler was unable to efficiently 292 explore the parameter space when the spectral indices were also 293

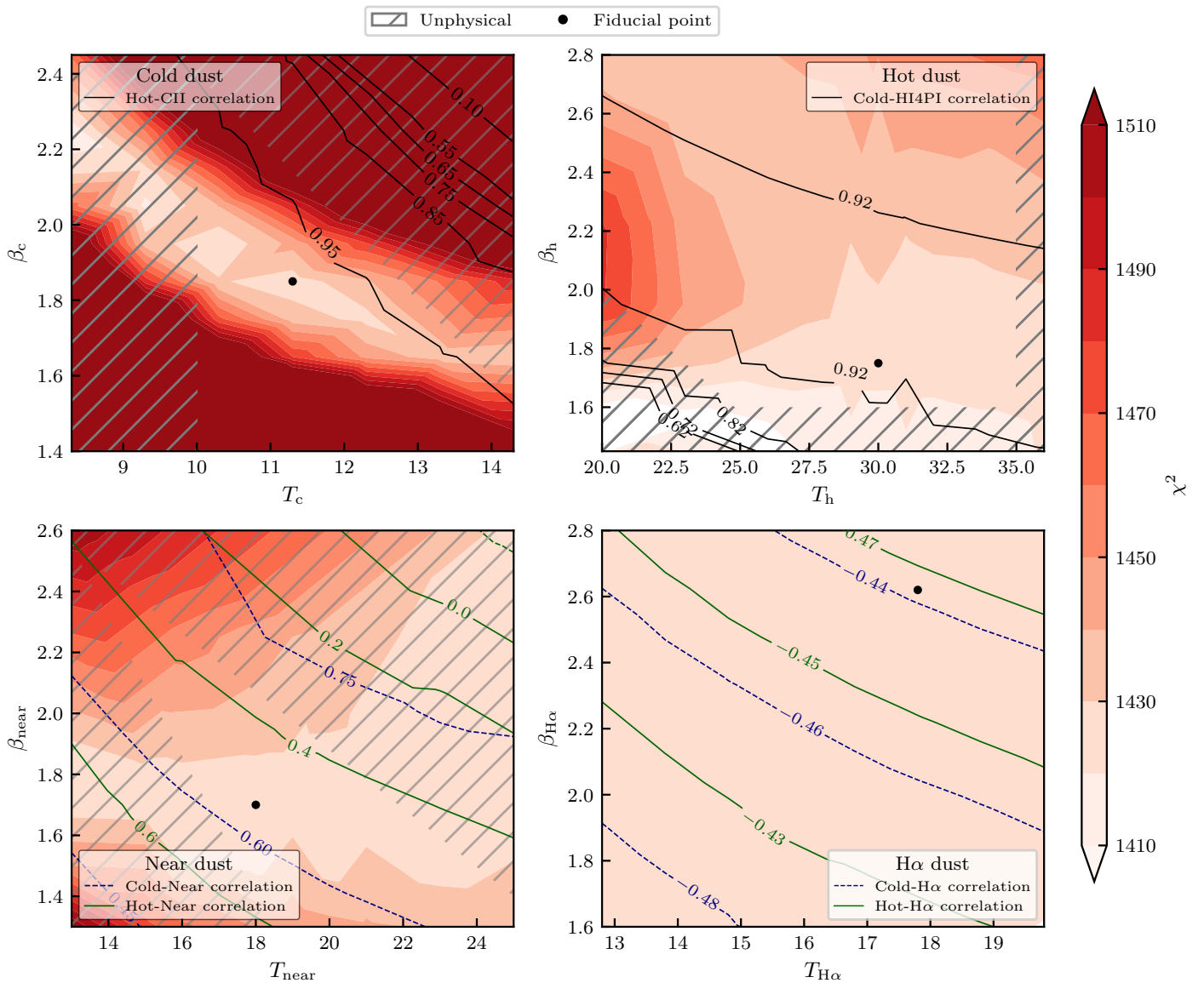


Fig. 2: Contour plot of relevant statistical tests and χ^2 for (clockwise from top left) cold dust, hot dust, H α dust and nearby dust. The black dot shows the fiducial point used for all parameters and grey grids mark the unphysical regions of the parameter space. Maps of a subset of the grid points can be found in [appendix D](#).

sampled in the Gibbs loop of [Sect. 4.1](#). To mitigate this, we performed an extensive grid search to explore the parameter space instead, while imposing a physicality prior that required the large scale amplitudes of the hot and cold dust to be positive. We also required that the temperatures of the dust component's MBB T did not exceed 35 K or go below 10 K, based on existing studies of dust environments that strongly disfavour more extreme conditions ([Hocuk et al. 2017](#); [Klessen & Glover 2016](#); [Hensley & Draine 2021](#)). Additionally, the nearby dust and the H α dust should be maximally uncorrelated with the hot and the cold dust. A highly correlated hot and nearby dust model might indicate, for example, that the nearby dust is too low, leaving nearby dust to leak into the hot dust. Lastly, we expect that the cold dust and the H α signal as seen by HI4PI should be more highly correlated, so we keep that in mind while exploring the parameter space (though we do not force such a correlation).

Each step in the grid search used Gibbs sampling to fit the per-channel 857 gains, the amplitudes per pixel of the hot and cold dust, the CMB and the CO amplitudes, as well as

monopoles and dipoles, for a set of fixed spectral parameters. These amplitudes are fit through the conjugate gradient sampling routine implemented in the Commander3 ([Galloway et al. 2023](#)) framework, and, as described above, given a fixed β and T for each dust component and a fixed amplitude scale for the templates. We then compare the χ^2 from the residuals, the correlations between the nearby-hot, nearby-cold, H α -hot and H α -cold maps, the correlation between the cold and HI4PI maps, and inspect the hot and cold maps for large scale negative amplitudes. We use this grid to find our best fit results and error estimates (see [Figs. 2 and 3](#) and [appendix D](#)).

5. Thermal dust template results

The grid search results are summarized in [Fig. 2](#). We show the χ^2 and relevant correlations contours for each set of parameters, assuming the fiducial value for the rest (see also [appendix D](#)). The grey grids show areas that were unphysical (with large negative hot or cold dust fits). We additionally plot the correlation

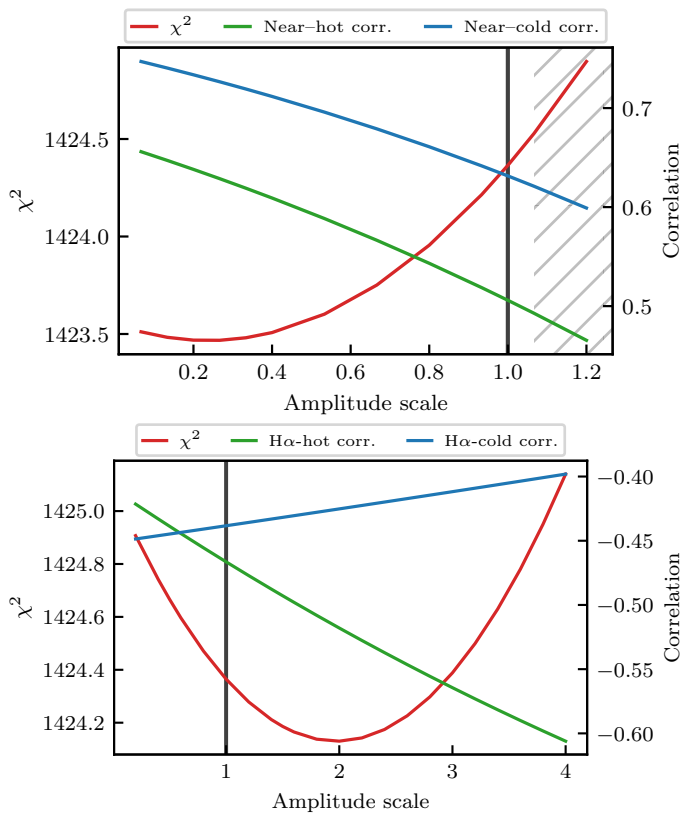


Fig. 3: χ^2 as a function of nearby (top) and $H\alpha$ correlated (bottom) dust amplitude scale. Note that the range of the scale of the χ^2 axes are very small.

with the hot and the cold dust compared to the templates for the nearby and $H\alpha$ correlated dust, where the aim is to have the lowest overall correlation between those components. We found that varying the spectral parameters of the hot or cold dust had a large effect on the final amplitudes of the other. For example, as the hot dust changed in temperature, the final amplitudes of the hot dust did not change drastically, however, the cold dust amplitudes did change dramatically in response. As such, we have included in the hot dust grid the correlation between the cold dust and the HI4PI maps, and interestingly the line tracing the 92% correlation traces closely with the unphysical region. A similar line can be drawn when we look at the correlation between the hot dust and the FIRAS C II map, with the 95% correlation region tracing the unphysical area. For the two template maps, the nearby and $H\alpha$ dust, we additionally explore the space of amplitude scale factors. This is simply a multiplicative factor applied to the template map, scaling the power up and down equally across the sky (see Fig. 3). For the nearby dust we again want to reduce the correlation between it and the hot and cold dust as much as possible, while satisfying the other physicality requirements discussed earlier. Broadly speaking, we have very little constraining power on the $H\alpha$ correlated dust with the *Planck* HFI bands. Since it represents a very small contribution to the signal, we choose to set the value of $T_{H\alpha}$ and $\beta_{H\alpha}$ to those from the DIRBE results (Gjerløw et al. 2026a). Despite exploring a wide parameter space for those and the amplitude scale factor, we found that the χ^2 and correlations with the hot and cold dust were relatively constant across the entire region.

The amplitude maps for the fiducial model can be seen in the top two panels of Fig. 4 and for the templates in Fig. B.1. It is

striking that even though the amplitudes were free to vary and take on any morphology they preferred, the shape of the cold dust closely resembles the $H\alpha$ map, shown in the bottom left panel. The cold dust is concentrated in the plane of the galaxy, but is still significant at high galactic latitudes. The shape of the hot dust also bears a striking resemblance to the lower resolution C II map in the bottom right panel. There is a clear excess closer to the galactic center, with small bubbles (e.g. the gum nebula at $l = 256^\circ, b = -9^\circ$) matching in both maps. This will be discussed further in Sect. 7.

The best fit MBB parameters are recorded in Table 1, where the error bars are interpreted from the grid search results in Fig. 2. In Gjerløw et al. (2026a) we found cold dust temperatures (corresponding to the CO and $H\alpha$ dust) of 12 and 16 K, with spectral indices of 1.9 and 1.4, so we find consistency between the HFI channels and the CO correlated dust of that analysis. The hot dust as fit by HFI is slightly hotter (at 30 K) than the fit from DIRBE templates (found to be 24.7 K), but with a relatively wide error bar they are still consistent. As mentioned previously, the $H\alpha$ correlated dust parameters were taken directly from the DIRBE template fits, and thus are consistent by construction. Lastly, the nearby dust (known as the *Gaia* extinction in Gjerløw et al. (2026a)) was found to have a slightly hotter fit for the HFI channels, at 18 K with spectral index of 1.7 compared to 14.9 K and 2.37 from the DIRBE templates. This dust, unlike the cold and hot dust, is much less concentrated nearby the galactic plane, as is expected (see appendix B for the template fits and discussion).

Figure 5 shows the MBB fits as a function of frequency, with amplitudes set by the RMS amplitude of the map for sky cuts about the galactic plane (94% and 70% f_{sky}). This emphasizes both the challenge of doing such a fit with only HFI data (since within the bands fit by HFI the spectra are relatively flat) but also the incredible power additional data sets (such as the Edenhofer et al. (2024) and Haffner et al. (2003, 2016)) bring, allowing us to effectively separate these dust components. A different visualization of the SEDs (spectral energy densities), the relative fraction of each dust component at 545 GHz, can be seen in Fig. E.1 and discussion in appendix E.

Results for the gain estimation for the fiducial model can be seen in Table 2. The 857 GHz gain values have a large impact on the dust, since they shift the measured spectrum in those bands, and the higher frequencies give us the longest “lever” on the dust (see again Fig. 5). They are very difficult to control and have a large error range as published by the *Planck* collaboration (Planck Collaboration LVII 2020). This is a major contributor to our error budget on the dust parameters.

The sky component fits can be seen in Fig. 6. Here, we have been able to recover the CMB with great accuracy, with minimal residuals, even in the galactic plane. The free-free is a fixed input template, and the recovery of the CO lines is sufficient for this analysis. The recovery of the CO line could be greatly improved in a future analysis where we allow the line ratios to fluctuate and include *Planck* LFI data to better control the low-frequency foregrounds.

Finally, the monopole values are simply offsets for each map, which are effectively a correction term for any residual offset that might have been introduced during map-making, and as such are not presented here due to space constraints.

6. Efficiency assessment and goodness-of-fit

We can assess our goodness-of-fit by comparing our model to the data – model residuals, as has been done in Fig. 7. The first col-

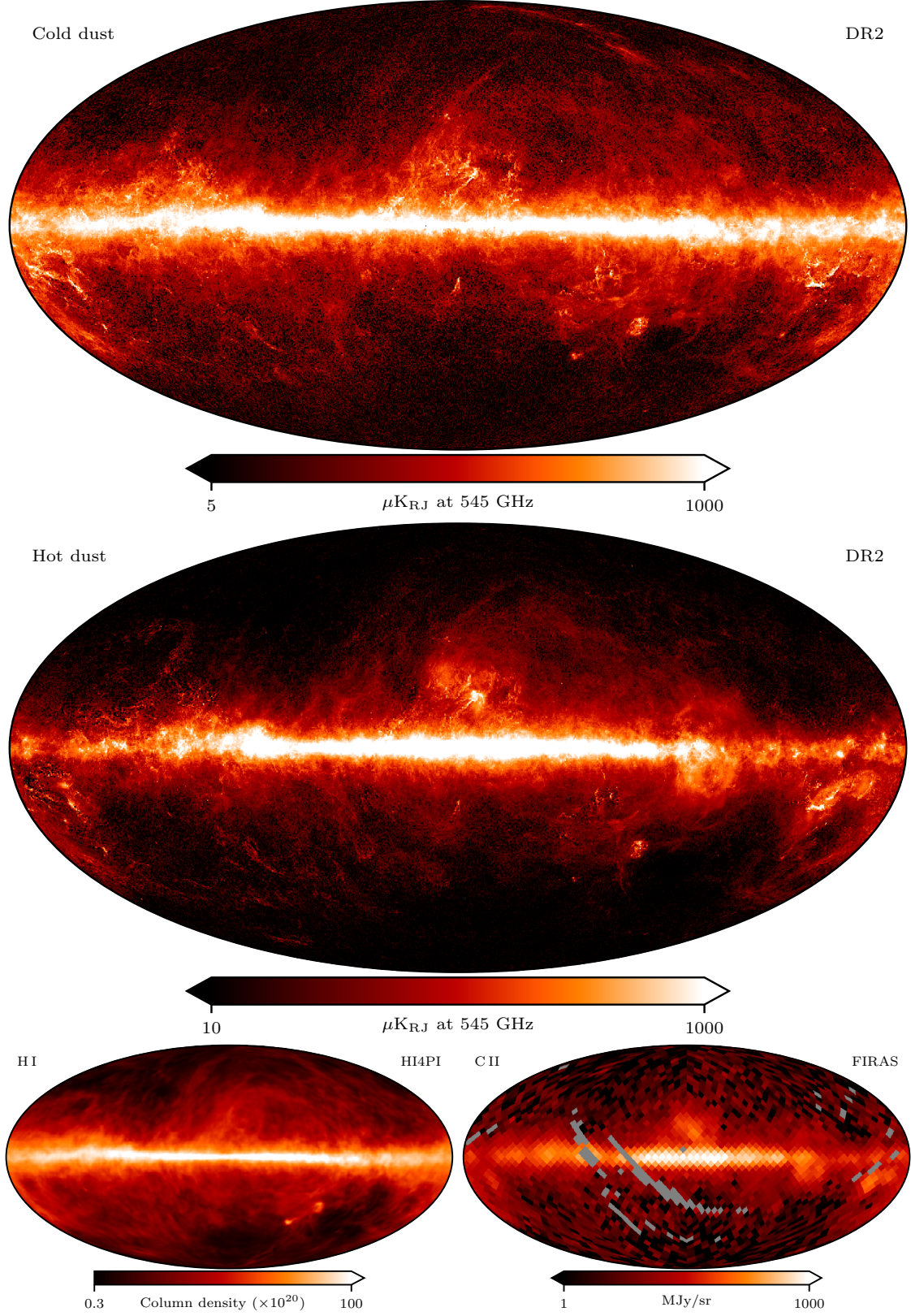


Fig. 4: DR2 Cold and hot dust components (top panels) as compared with relevant tracers HI and C II (bottom panels).

umn is the sum of all dust maps and residuals at each of the six *Planck* HFI frequencies. The central column shows the residuals at the same scale range as the maps, and the right column shows the residuals at a factor of 100 smaller scale range. While there is still structure to the residual maps, they are largely driven by

structures that appear uncorrelated with galactic dust. This indicates there are perhaps future improvements to be made to the gain, zodiacal light modelling and potentially carbon monoxide lines. The residuals for each individual detector can be found in [appendix C](#).

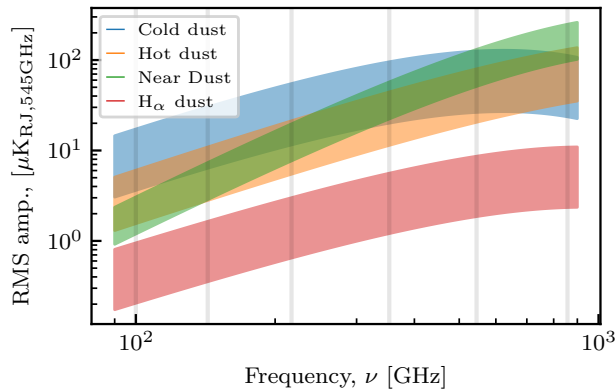


Fig. 5: Spectral energy density (SED) for the four dust components across the HFI bands. Note that the H_α dust is a negative amplitude since it is an extinction component, but the absolute value is plotted for clarity. The lower bound is set by a 70% f_{sky} and the upper bound by a 94% f_{sky} . The grey vertical lines are the locations of the 6 *Planck* HFI bands.

432 To quantify this residual level, Fig. 8 compares the summed
 433 dust components and residuals to the residual map, normalized
 434 by the input dust map. This tells us what fraction of the dust
 435 signal has been successfully modelled by this approach, and we
 436 see that the four-component dust model is able to account for
 437 over 99% of the dust signal across all six *Planck* HFI bands.

438 7. Correlations with external line emission maps

439 One of the great successes of this four-component dust model is
 440 the high degree of correlation between the dust components and
 441 physical tracers. The H_1 emission, a known dust tracer, and the
 442 cold dust have a Pearson's correlation coefficient of 92%, and the
 443 hot dust and the new dust tracer C II, which traditionally maps the
 444 hot ionized medium, have a correlation of 95%. Fig. 9 shows per-
 445 pixel scatter plots between our dust maps and these tracers. The
 446 top panel shows the hot dust and FIRAS C II, downgraded to the
 447 7° resolution of the FIRAS maps, and the bottom panel shows
 448 the cold dust and HI4PI column density maps at $N_{\text{side}} = 1024$.
 449 Both show strong correlation, which is further evidence that they
 450 trace similar regions of the Galaxy.

451 Visually, we can also consider the top two panels of Fig. 4
 452 and compare by eye with the bottom two sub-panels. Several
 453 striking features can be seen to be present both in the cold dust
 454 and the HI4PI, as well as in the hot dust and the FIRAS C II
 455 maps. It is evident that these are tracers of our dust components,
 456 and potentially future analysis could use C II maps to even better
 457 constrain the hot dust, as an additional external data set.

458 Evidence for this correlation is further supported by the ob-
 459 servation of an interesting feature in the hot and cold dust grids
 460 (Fig. 2). The areas where the resulting maps looked unphysi-
 461 cal also trace regions in parameter space where the correlation
 462 between the dust and their relevant tracer were lower (e.g. the
 463 95% Hot-C II contour line traces the grey gridded region in the
 464 cold dust χ^2 contour plot, and the 92% Cold-H I contour line also
 465 maps the excluded region in the hot dust plot). Since these tracers
 466 are not included in the fitting, and are simply calculated from the
 467 resulting maps, it appears that these phenomena arise in tandem.
 468 Dust models which have lower levels of physical correlations
 469 between the dust and the tracers produce unphysical results else-
 470 where in the model, further supporting the conclusion that these
 471 correlations are an important and physical part of the model.

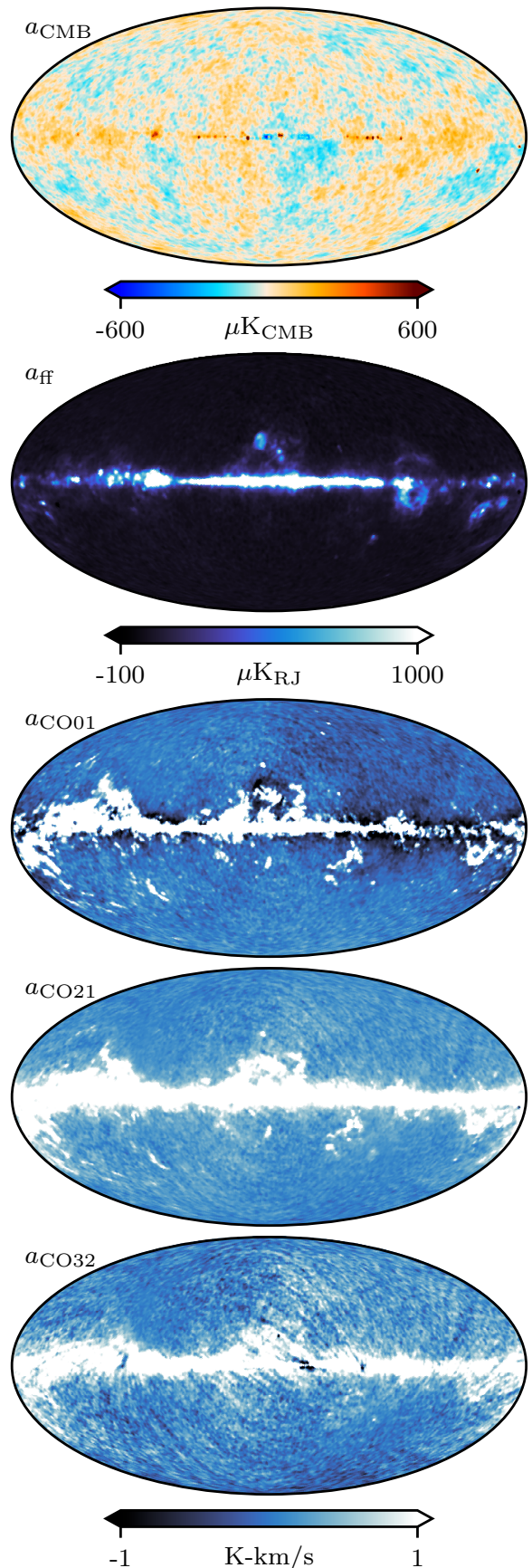


Fig. 6: Sky model amplitude maps corresponding to the baseline thermal dust model. From top to bottom, the panels show CMB, free-free, CO $J = 1-0$, CO $J = 2-1$, and CO $J = 3 - 2$. All maps are smoothed to a common resolution of 80' FWHM.

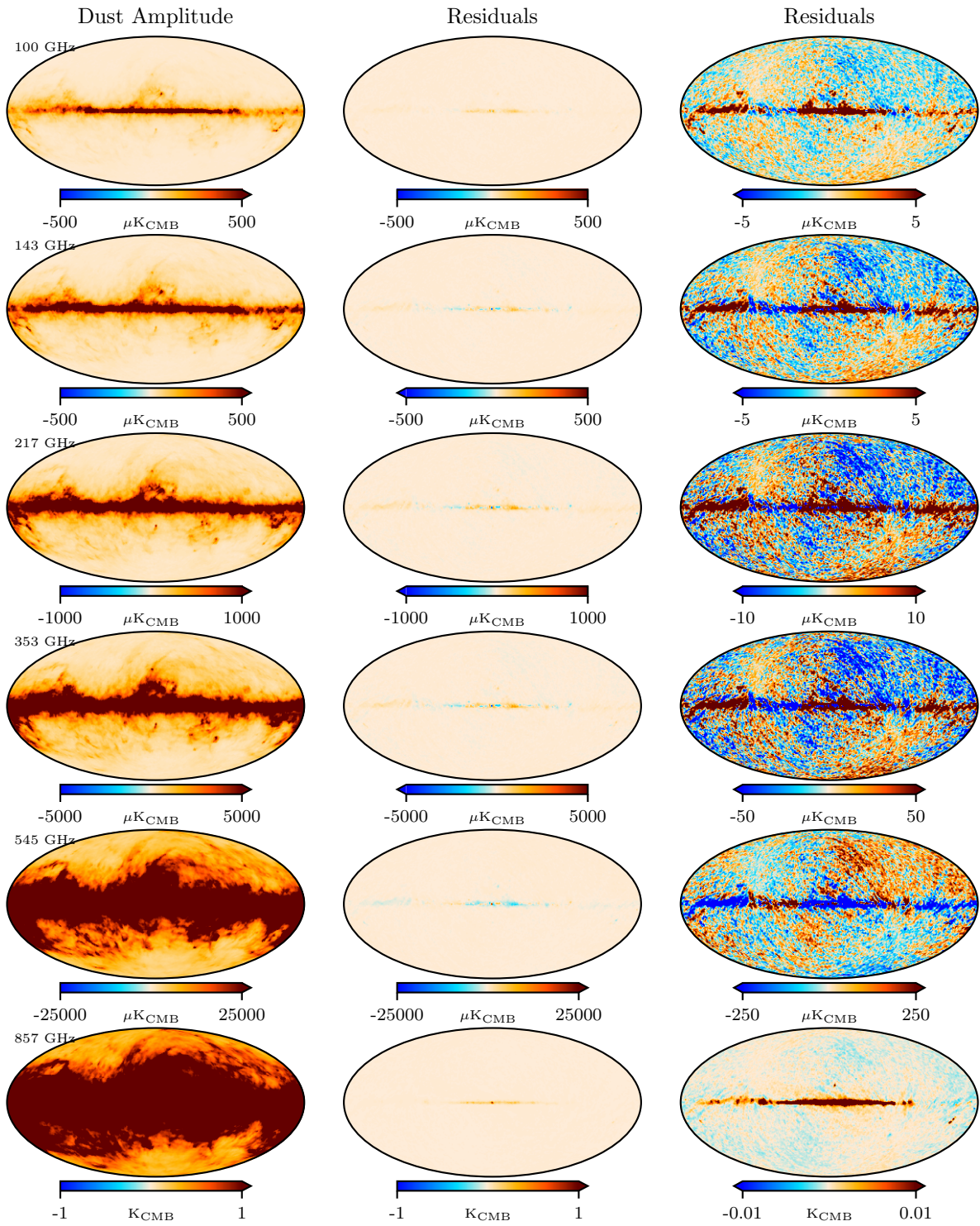


Fig. 7: Left column shows the sum of the dust maps averaged for each band (plus their residuals), and the middle column the corresponding residuals (with the same colour bar range). The final column shows the residuals with the colour bar scaled down by a factor of 100 to more easily see the structure in the residuals. All the maps have been smoothed by 2 degrees for clarity.

472 Figure 10 shows the full set of spatial correlations between
 473 the different dust components and tracers, and we can see that
 474 we have a low degree of correlation between the nearby dust and
 475 the hot and cold dust. As previously mentioned, the hot and C II
 476 components show 95% correlation, and the cold and HI4PI maps
 477 are correlated at the 92% level, but we also see that the hot and
 478 cold components are correlated at the 80% level. Correlations
 479 between C II and H I have been known and discussed regarding

480 gas populations in the Milky Way galaxy Langer et al. (2014, 481
 482 2010); Pineda et al. (2013), so seeing the same effect between
 481 the hot and cold dust here is not unexpected.

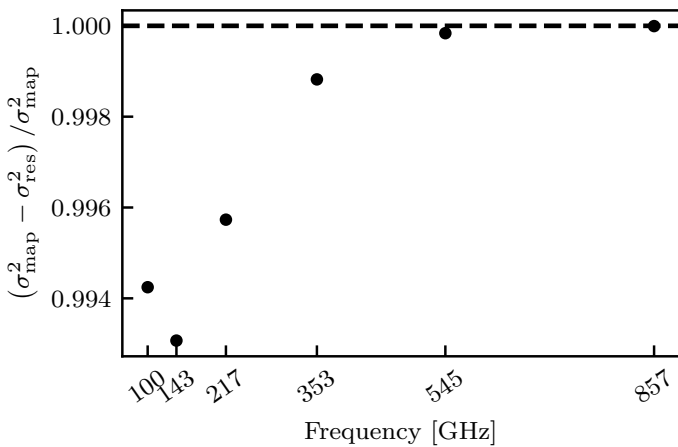


Fig. 8: Efficiency of the dust model at representing the data. Along the y-axis we plot result from the input map minus the non-dust components (e.g. CMB, free-free, CO) squared minus the residuals squared, divided by the residuals squared. This informs how much of the signal is represented by the model and we find that it is greater than 99% across all HFI bands.

8. Modified blackbody fit to multi-component dust model

So far we have fit four dust components to the *Planck* data, each modelled as a modified black-body with free global spectral parameters T and β (constant across the sky). We now want to compare this to the *Planck* 2015 (Planck Collaboration X 2016) analysis where only one MBB dust component was fit to the *Planck* data, but with spatial variations of T and β allowed. The *Planck* 2015 maps are plotted at the top of Fig. 11. Here both T , β , and the dust amplitude are fitted per HEALPix $N_{\text{side}} = 256$ pixel using Commander1 (Eriksen et al. 2008).⁷ While β is relatively flat on the sky, we see that T varies significantly. Note that in Planck Collaboration X (2016) CIB was not fitted separately, and the CIB fluctuations, therefore, mostly went into the thermal dust component. The hot areas at high Galactic latitudes corresponds to CIB mixing in the dust component.

Planck Collaboration Int. XLVIII (2016) fit separate CIB and thermal dust components to the *Planck* data using GNILC, a needlet internal linear combination code with power spectrum priors. Here, the thermal dust component was also modelled as a one-component MBB with variable T and β as plotted in the middle of Fig. 11. Compared to the Commander maps above, the CIB contamination is now gone from the T map, but the β map varies more on the sky.

In the bottom of Fig. 11 we have used Commander 1 to fit a one-component MBB with varying spectral indices to the four-component dust model with spatially flat spectral parameters, as developed in this paper. We see that an underlying simple four-component dust model appears very similar to a one-component model with a nearly constant β and a varying temperature T . Except at high latitudes, where the *Planck* 2015 T map is CIB dominated and the current analysis subtracts CIB fluctuations at the input map level, the two T maps agree very well. This shows that the effective one-component MBB from *Planck* 2015

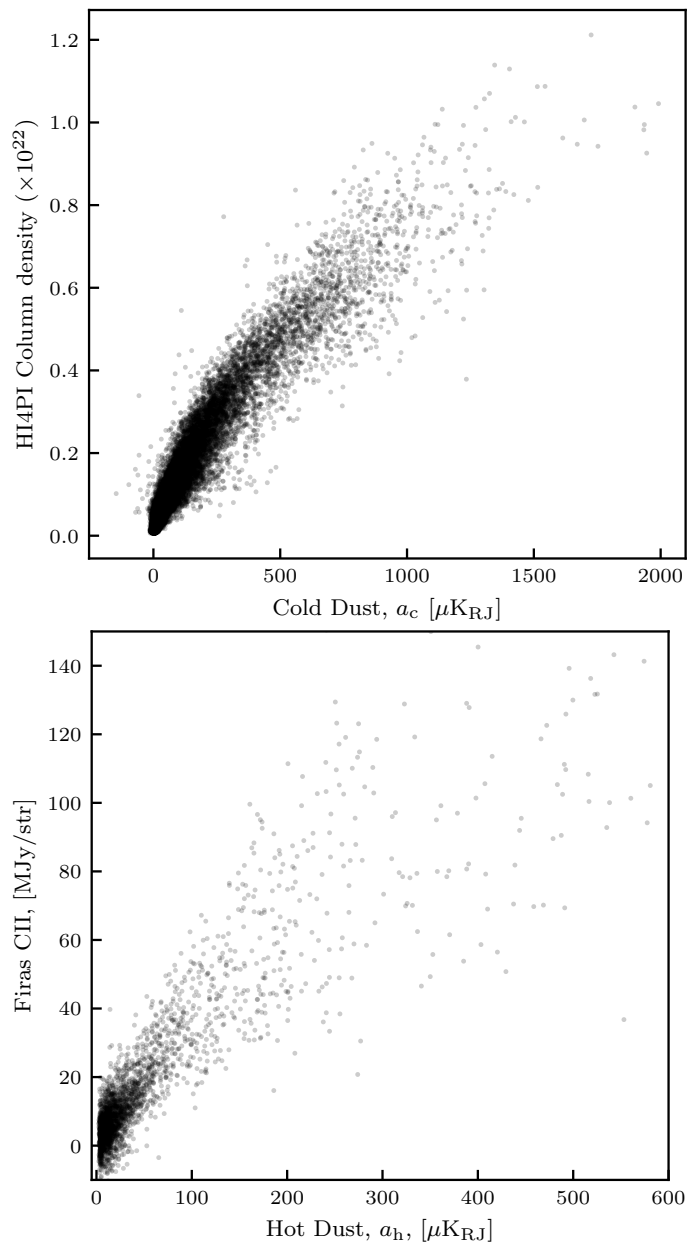


Fig. 9: Top: Scatter plot between the hot dust and FIRAS C II maps; both maps are smoothed to a common resolution of 420' FWHM, and pixelated at $N_{\text{side}}=16$. Bottom: Scatter plot between the cold dust and HI4PI maps; both maps are smoothed to a common resolution of 16.2' FWHM, and pixelated at $N_{\text{side}}=1024$.

can instead be replaced with the new, simpler, four-component model, which in fact has fewer free parameters per pixel. 517
518

9. Conclusions

In Gjerløw et al. (2026a) we showed that the thermal dust in the microwave and infrared regimes could be described well by a multi-component model, in which each component is tracing a specific physical environment. Namely, we use templates to trace H₁ correlated dust, C II correlated dust, stellar extinction dust, CO correlated dust and H α correlated dust, and perform a low-resolution analysis with these templates. We found that this fit a modified blackbody across most of the included bands and had little spatial SED variations. Two dominant components found

⁷ Commander1 is distinct from Commander3 in that it uses a per-pixel Gibbs sampling routine, compared to the Commander3, which mixes harmonic and map space analysis allowing for multi-resolution analysis.

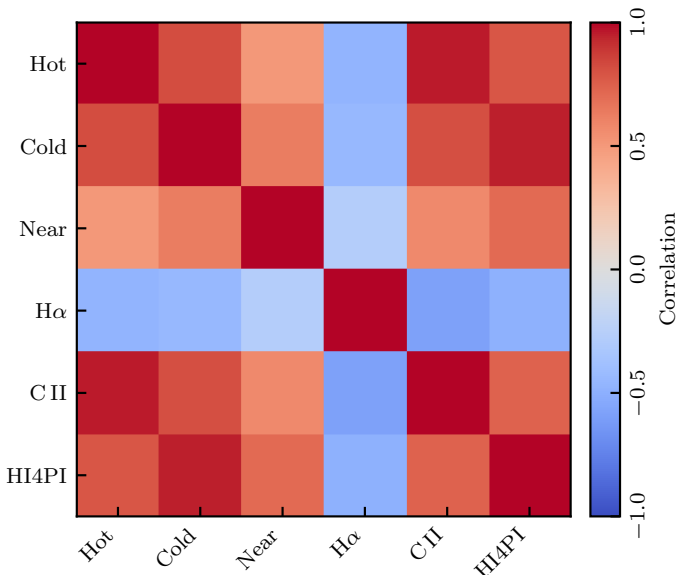


Fig. 10: Pearson's correlation coefficient between dust components and tracers. The correlation between the hot dust and the C II emission seen in FIRAS, as well as the cold dust and the HI4PI H I emission are very strong.

in Gjerløw et al. (2026a) were the C II correlated dust (hot dust) and the H I correlated dust (cold dust). The correlation between C II emission and dust had not been previously known to us, but represented an exciting new tracer.

Here, we present the first high resolution four-component dust maps produced using the *Planck* HFI data. We generate two novel dust maps, corresponding to the hot and cold dust populations, which have global temperature and spectral indices of $T_h = 30$ K, $\beta_h = 1.75$, and $T_c = 11$ K, $\beta_c = 1.85$ respectively. These maps have a 92% correlation between the cold dust and the HI4PI map (HI4PI Collaboration et al. 2016) and a striking 95% correlation between the hot dust and the FIRAS C II map. This new dust model is able to successfully map physical tracers of hot and cold regions in the Milky Way, with fewer free parameters than previous dust models, and with more physical meaning to the parameters. We believe that this model represents a strict improvement over the established 3-parameter MBB description of dust and should be used preferentially for future simulations of Milky Way dust.

When compared to previous *Planck* dust maps, by combining the four dust templates into a single dust component, we see similar results, without large spatial SED variations. This strongly suggests that previous analyses that have modelled dust as a one-component MBB with spatially varying spectral indices have actually been averaging over different effects that ideally should not be averaged over. As such, by using multiple components with simpler spatial variations, our model is a simpler, more physical, and more economical. Furthermore, as it is computationally much easier to fit for linear (amplitude) parameters than for non-linear (spectral) parameters, so this will also provide speed-ups to future dust simulations and analysis.

In the future, this work should be extended through joint analyses with DIRBE, AKARI, WISE, SPHEREx and others, to produce even higher resolution dust maps with greater sensitivity and longer frequency coverage. This result is also critically important for polarization B-mode experiments, as it may suggest that future polarization B-mode experiments should implement

capabilities to disentangle hot and cold dust efficiently, which suggest requiring data with their highest frequency around 800–1000 GHz.

Acknowledgements. The current work has received funding from the European Union's Horizon 2020 research and innovation programme under grant agreement numbers 819478 (ERC; COSMOGLOBE) and 772253 (ERC; BITS2COSMOLOGY). Some of the results in this paper have been derived using the HEALPix (Górski et al. 2005) package. We acknowledge the use of the Legacy Archive for Microwave Background Data Analysis (LAMBDA), part of the High Energy Astrophysics Science Archive Center (HEASARC). HEASARC/LAMBDA is a service of the Astrophysics Science Division at the NASA Goddard Space Flight Center. This publication makes use of data products from the Wide-field Infrared Survey Explorer, which is a joint project of the University of California, Los Angeles, and the Jet Propulsion Laboratory/California Institute of Technology, and NEOWISE, which is a project of the Jet Propulsion Laboratory/California Institute of Technology. WISE and NEOWISE are funded by the National Aeronautics and Space Administration. This work has made use of data from the European Space Agency (ESA) mission *Gaia* (<https://www.cosmos.esa.int/gaia>), processed by the *Gaia* Data Processing and Analysis Consortium (DPAC, <https://www.cosmos.esa.int/web/gaia/dpac/consortium>). Funding for the DPAC has been provided by national institutions, in particular the institutions participating in the *Gaia* Multilateral Agreement. This paper and related research have been conducted during and with the support of the Italian national inter-university PhD programme in Space Science and Technology. Work on this article was produced while attending the PhD program in PhD in Space Science and Technology at the University of Trento, Cycle XXXIX, with the support of a scholarship financed by the Ministerial Decree no. 118 of 2nd March 2023, based on the NRRP - funded by the European Union - NextGenerationEU - Mission 4 "Education and Research", Component 1 "Enhancement of the offer of educational services: from nurseries to universities" - Investment 4.1 "Extension of the number of research doctorates and innovative doctorates for public administration and cultural heritage" - CUP E66E23000110001.

References

- Ade, P., Aguirre, J., Ahmed, Z., et al. 2019, J. Cosmology Astropart. Phys., 2019, 056
 Ade, P. A. R., Aikin, R. W., Barkats, D., et al. 2014, Physical Review Letters, 112, 241101
 BeyondPlanck Collaboration. 2023, A&A, 675, A1
 BICEP2 Collaboration. 2018, Phys. Rev. Lett., 121, 221301
 Cutri, R. M., Wright, E. L., Conrow, T., et al. 2013, Explanatory Supplement to the All-WISE Data Release Products, Explanatory Supplement to the All-WISE Data Release Products, by R. M. Cutri et al.
 Dame, T. M., Hartmann, D., & Thaddeus, P. 2001, ApJ, 547, 792
 Díaz-Santos, T., Armus, L., Charmandaris, V., et al. 2017, ApJ, 846, 32
 Edenhofer, G., Zucker, C., Frank, P., et al. 2024, A&A, 685, A82
 Eriksen, H. K., Jewell, J. B., Dickinson, C., et al. 2008, ApJ, 676, 10
 Finkbeiner, D. P., Davis, M., & Schlegel, D. J. 1999, ApJ, 524, 867
 Fixsen, D. J., Weiland, J. L., Brodd, S., et al. 1997, ApJ, 490, 482
 Gaia Collaboration et al. 2016, A&A, 595, A1
 Galloway, M., Andersen, K. J., Aurién, R., et al. 2023, A&A, 675, A3
 Galloway, M. et al. 2026, A&A, in preparation [arXiv:20xx.xxxxx]
 Geman, S. & Geman, D. 1984, IEEE Trans. Pattern Anal. Mach. Intell., 6, 721
 Gjerløw et al. 2026a, A&A, in preparation [arXiv:20xx.xxxxx]
 Gjerløw et al. 2026b, A&A, in preparation [arXiv:20xx.xxxxx]
 Górski, K. M., Hivon, E., Banday, A. J., et al. 2005, ApJ, 622, 759
 Haffner, L. M., Reynolds, R. J., Babler, B. L., et al. 2016, in American Astronomical Society Meeting Abstracts, Vol. 227, American Astronomical Society Meeting Abstracts #227, 347.17
 Haffner, L. M., Reynolds, R. J., Tufte, S. L., et al. 2003, ApJS, 149, 405
 Hauser, M. G., Arendt, R. G., Kelsall, T., et al. 1998, ApJ, 508, 25
 Hensley, B. S. & Draine, B. T. 2021, ApJ, 906, 73
 Hensley, B. S. & Draine, B. T. 2023, ApJ, 948, 55
 HI4PI Collaboration, Ben Bekhti, N., Flöer, L., et al. 2016, A&A, 594, A116
 Hocuk, S., Szűcs, L., Caselli, P., et al. 2017, A&A, 604, A58
 Jackson, J. M., Allingham, D., Killerby-Smith, N., et al. 2020, ApJ, 904, 18
 Juvela, M. & Ysard, N. 2012, A&A, 541, A33
 Kelsall, T., Weiland, J. L., Franz, B. A., et al. 1998, ApJ, 508, 44
 Klessen, R. S. & Glover, S. C. O. 2016, Saas-Fee Advanced Course, 43, 85
 Lallement, R., Vergely, J. L., Babusiaux, C., & Cox, N. L. J. 2022, A&A, 661, A147
 Langer, W. D., Pineda, J. L., & Velusamy, T. 2014, A&A, 564, A101
 Langer, W. D., Velusamy, T., Pineda, J. L., et al. 2010, A&A, 521, L17
 Lenz, D., Hensley, B. S., & Doré, O. 2017, ApJ, 846, 38

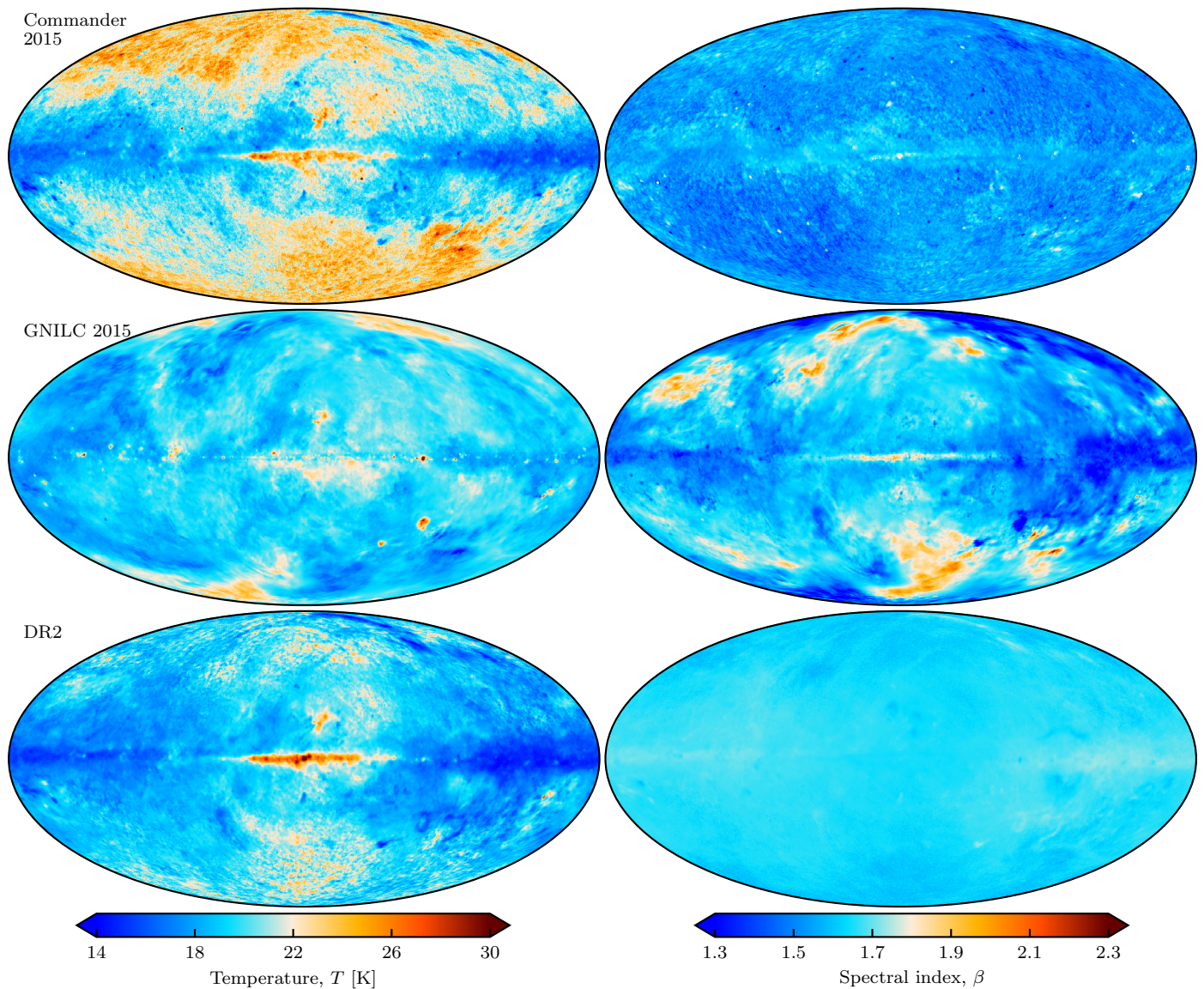


Fig. 11: Comparison of the temperature T and spectral index β sky fits between *Planck* 2015, *GNILC* 2015 and the new *COSMOGLOBE* DR2 results. Priors for the top and bottom plots are the same.

- | | |
|--|--|
| 640 LiteBIRD Collaboration, Ally, E., Arnold, K., et al. 2023, Progress of Theoretical
641 and Experimental Physics, 2023, 042F01
642 Maris, M., Burigana, C., & Fogliani, S. 2006, A&A, 452, 685
643 Mather, J. C., Cheng, E. S., Cottingham, D. A., et al. 1994, ApJ, 420, 439
644 Montegriffo, P., De Angeli, F., Andrae, R., et al. 2023, A&A, 674, A3
645 Partridge, R. B. & Peebles, P. J. E. 1967, ApJ, 148, 377
646 Penzias, A. A. & Wilson, R. W. 1965, ApJ, 142, 419
647 Pineda, J. L., Langer, W. D., Velusamy, T., & Goldsmith, P. F. 2013, A&A, 554,
648 A103
649 Planck Collaboration. 2018, arXiv e-prints, arXiv:1807.06212
650 Planck Collaboration X. 2011, A&A, 536, A10
651 Planck Collaboration VI. 2014, A&A, 571, A6
652 Planck Collaboration XI. 2014, A&A, 571, A11
653 Planck Collaboration XIV. 2014, A&A, 571, A14
654 Planck Collaboration VIII. 2016, A&A, 594, A8
655 Planck Collaboration X. 2016, A&A, 594, A10
656 Planck Collaboration IV. 2020, A&A, 641, A4
657 Planck Collaboration Int. XXV. 2015, A&A, 582, A28
658 Planck Collaboration Int. XXVI. 2015, A&A, 582, A29
659 Planck Collaboration Int. XLVIII. 2016, A&A, 596, A109
660 Planck Collaboration Int. LVI. 2020, A&A, 644, 100
661 Planck Collaboration Int. LVII. 2020, A&A, 643, 42
662 Planck Collaboration LVII. 2020, A&A, 643, A42
663 San, M. et al. 2024, A&A, in preparation [arXiv:20xx.xxxxx]
664 Skrutskie, M. F., Cutri, R. M., Stiening, R., et al. 2006, AJ, 131, 1163 | Wang, C., Huang, Y., Yuan, H., et al. 2022a, ApJS, 259, 51
Wang, L., Li, J., Wu, Y., et al. 2022b, VizieR Online Data Catalog: Classical
Be stars from LAMOST MRS DR7 (Wang+, 2022), VizieR On-line Data
Catalog: J/ApJS/260/35. Originally published in: 2022ApJS..260...35W
Watts, D., Galloway, M., Gjerlow, E., et al. 2024a, A&A, submitted
[arXiv:2408.10952]
Watts, D. et al. 2024b, A&A, in preparation [arXiv:2406.01491]
Wright, E. L., Eisenhardt, P. R. M., Mainzer, A. K., et al. 2010, AJ, 140, 1868
Xiang, M. & Rix, H.-W. 2023, VizieR Online Data Catalog (other), 0380,
J/other/Nat/603
Xiang, M., Rix, H.-W., Ting, Y.-S., et al. 2022, A&A, 662, A66
Zhang, X., Green, G. M., & Rix, H.-W. 2023, MNRAS, 524, 1855
Zonca, A., Singer, L., Lenz, D., et al. 2019, Journal of Open Source Software, 4,
1298
Zucker, C., Speagle, J. S., Schlafly, E. F., et al. 2019, ApJ, 879, 125 |
|--|--|

Appendix A: RMS scaling

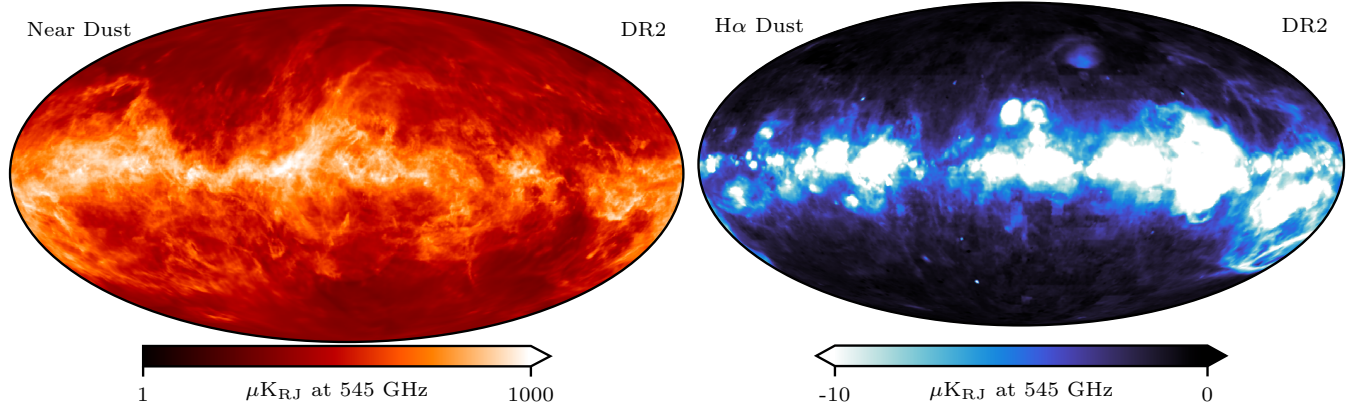
The published single horn RMS maps were found to have a known residual multiplicative offset from the production pipeline, as is evident when the single horn data maps and RMS maps are compared to each-other and to the single frequency maps (averaged maps). We include in Table A.1 the values used here to divide the single horn RMS maps.

Table A.1: RMS scales used in this analysis.

Frequency	Horn 1	Horn 2	Horn 3	Horn 4	Horn 5	Horn 6	Horn 7	Horn 8
100 GHz	1.414	1.414	1.414	1.414	-	-	-	-
143 GHz	1.85	2.1	2.03	1.88	1.68	1.6	1.75	-
217 GHz	1.414	1.414	1.414	1.414	1.0	1.0	1.0	1.0
353 GHz	1.0	1.0	1.414	1.414	1.414	1.414	1.0	1.0
545 GHz	3.2	3.25	-	3.05	-	-	-	-
857 GHz	9.8	10.6	10.3	8.0	-	-	-	-

Appendix B: Dust templates

The templates used for the nearby dust and the H α dust are the stellar dust extinction from Edenhofer et al. (2024) and the WHAM maps (Haffner et al. 2003, 2016). The fits from this analysis can be seen in Fig. B.1. Note that the H α dust is negative as it represents a dust extinction component for the HFI bands, reducing the apparent dust in the blue areas. The nearby dust is mapped out to 1.25 kpc from the Sun, and has a higher amplitude away from the galactic plane when compared to the other dust components (see also appendix E).

Fig. B.1: Nearby dust and H α dust extinction template fits.

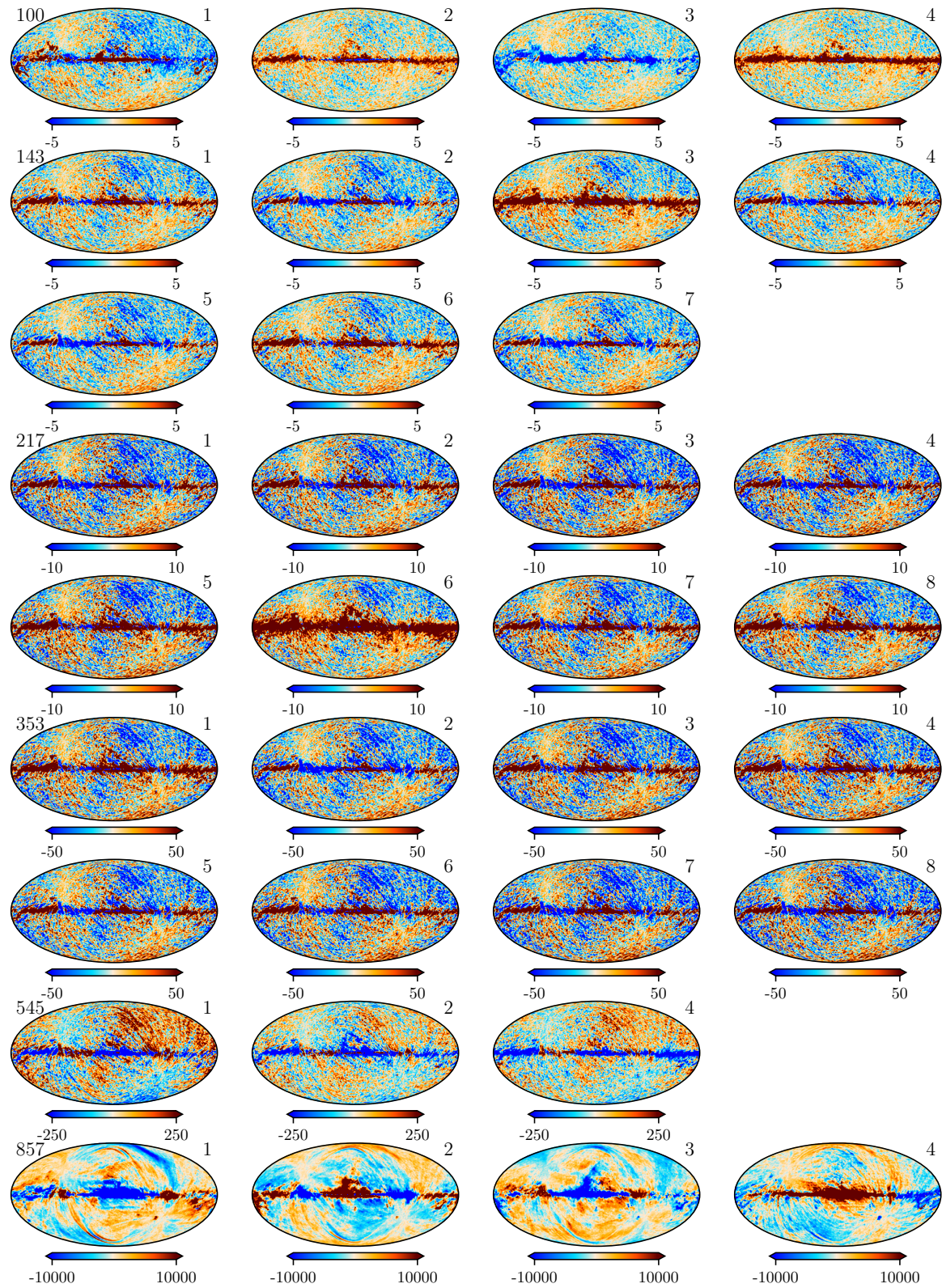
690 **Appendix C: Residuals**

Fig. C.1: Residuals (Data minus model) for the *Planck* HFI bands. Units are in μK_{CMB} . The residuals hint at some uncorrected zodiacal light along the ecliptic plane, as well as potentially some offsets to the gain of the 545 channels.

692 We can see the fidelity of the sky model by looking at the difference between the data and the model at each of the bands (see
 693 Fig. C.1). The residuals indicate potential for improvement to the modelling of the zodiacal light, as well as improvements to the
 694 545 GHz gain. The incredibly low residuals in the 100, 143, 217 and 353 GHz maps demonstrate the success of this model.

Appendix D: Grid search tests

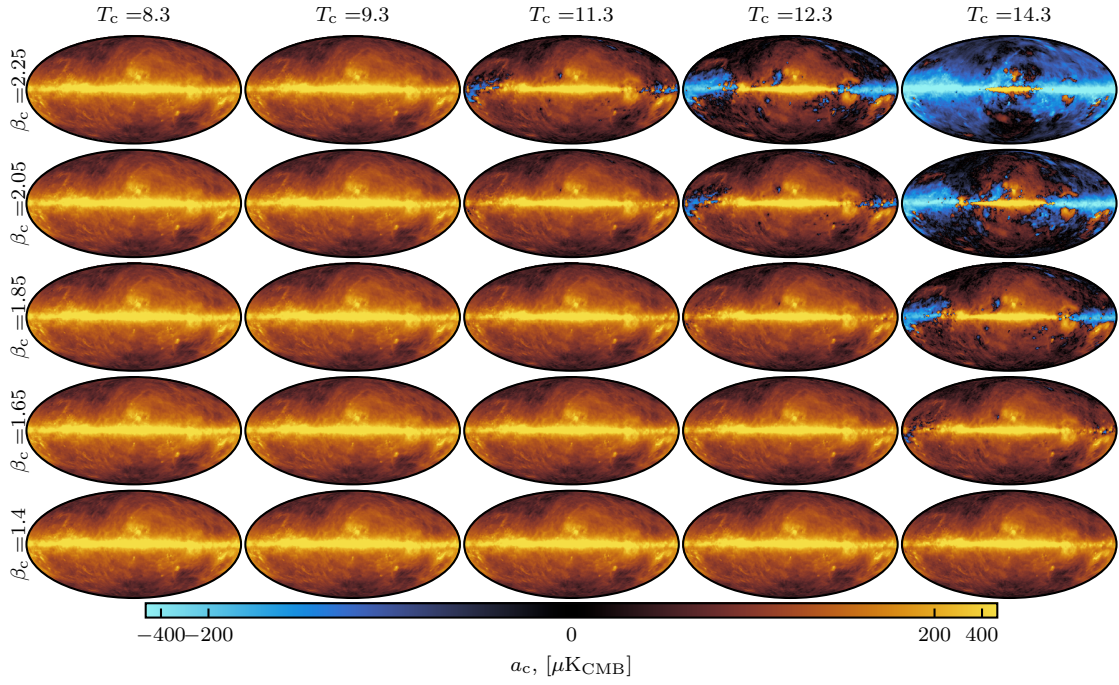


Fig. D.1: Hot dust amplitudes for varying T_c and β_c values with all other grid parameters set to the fiducial values as recorded in Table 1. The center panel is the fiducial map. The corresponding cold dust maps ratios can be seen in Fig. D.2.

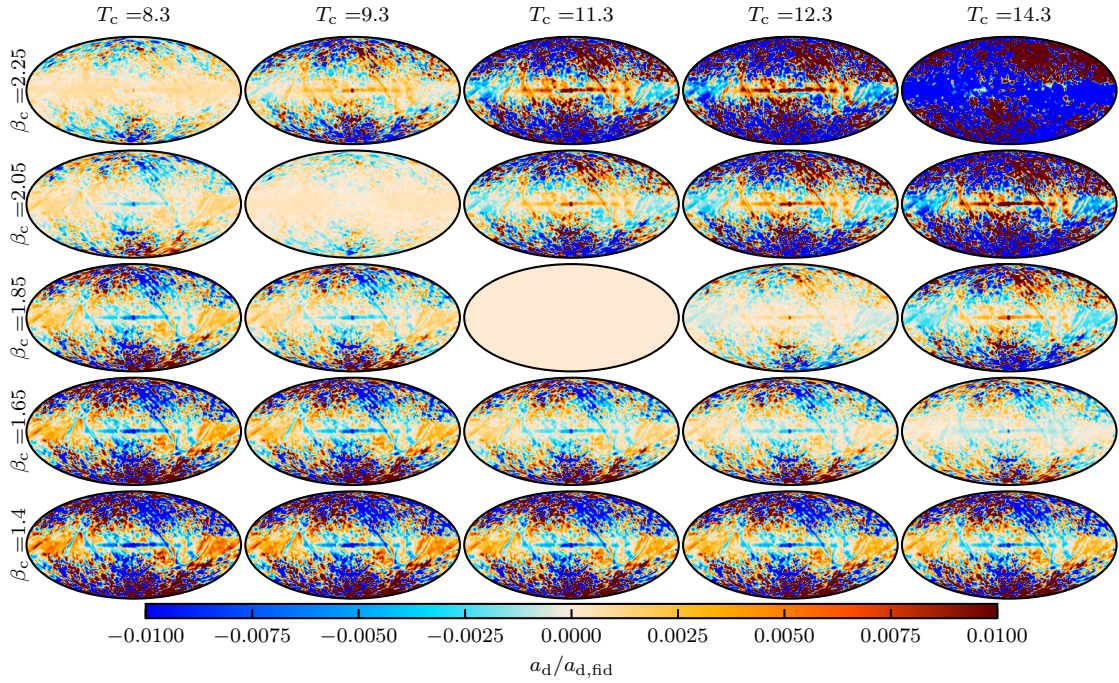


Fig. D.2: Monopole subtracted ratio of the cold dust amplitudes compared to the fiducial value (central panel) for varying T_c and β_c . The corresponding hot dust maps can be seen in Fig. D.1.

We plot several of the maps from the grid search in Sect. 5. Since the H α dust and nearby dust are templates they do not change by eye (only scaling by a set factor for each frequency given a set of T, β, a) so they are not plotted here. Thus, we plot the amplitudes of the cold and hot dust for each of the grid points. We show a sample for each of the grids in Fig. 2 with the central map the fiducial point and varying the spectral index along the vertical axis and the temperature along the y-axis.

Appendix D.1: Cold dust

697
698
699
700

As can be seen in Fig. 2, there is an unphysical space mapped by the hottest and highest spectral indices in the cold dust grid. This corresponds to large over-subtraction and negative areas in the hot dust amplitudes as can be seen in Fig. D.1. When shifting the

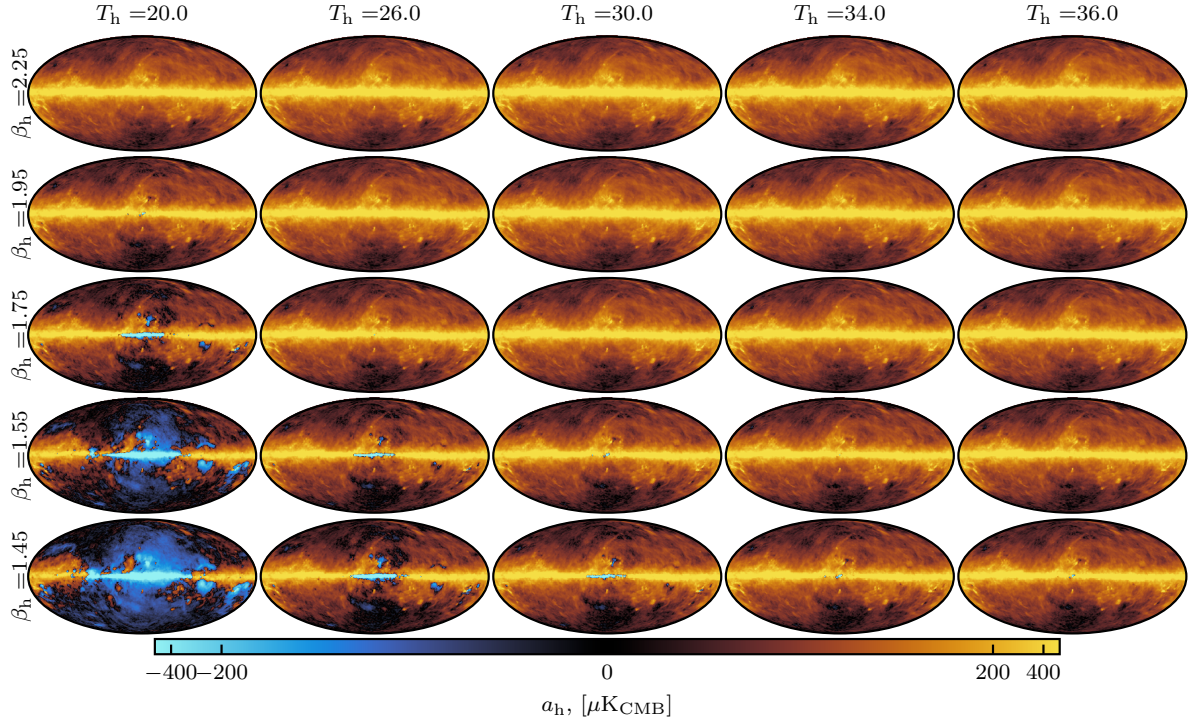


Fig. D.3: Cold dust amplitudes for varying T_h and β_h values with all other grid parameters set to the fiducial values as recorded in Table 1. The central panel is the fiducial map. The corresponding hot dust maps ratios can be seen in Fig. D.4.

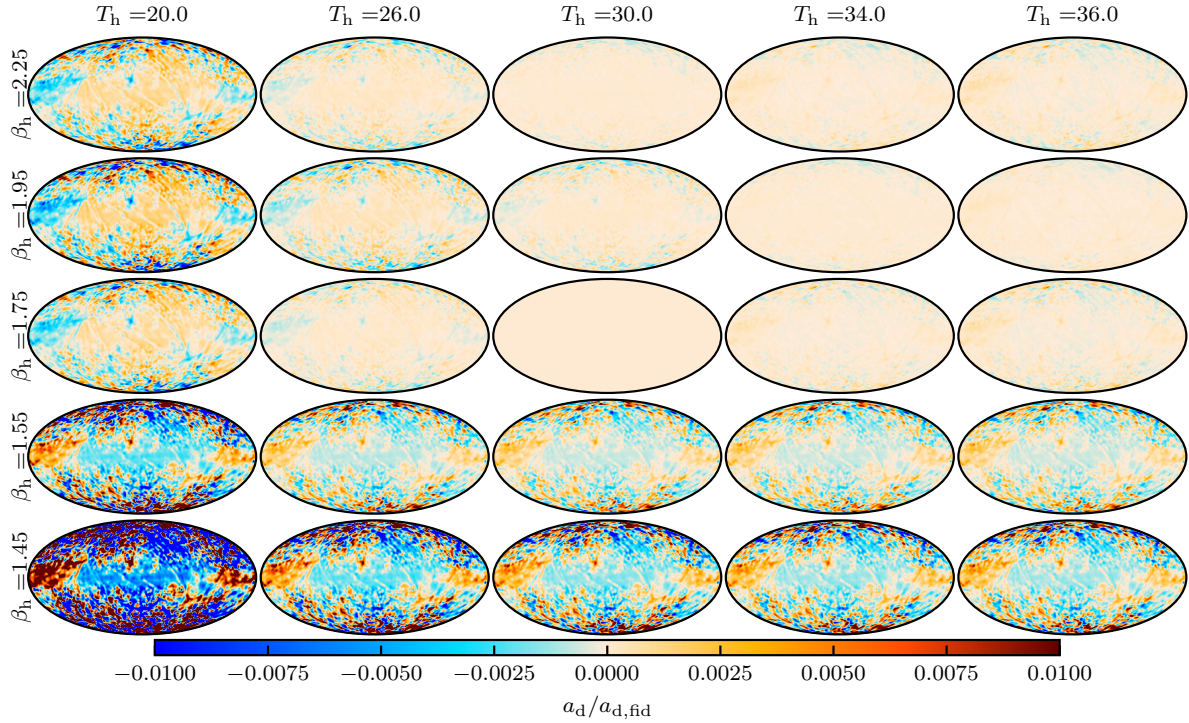


Fig. D.4: Monopole subtracted ratio of the hot dust amplitudes compared to the fiducial value (central panel) for varying T_h and β_h . The corresponding cold dust maps can be seen in Fig. D.3

704 T_c and β_c , we find the shape of the amplitude maps is visually similar to the fiducial map (see Fig. 4), so we show the monopole
 705 subtraction of the grid position to the fiducial value in Fig. D.2.

706 Appendix D.2: Hot dust

707 Similar to with the cold dust, in Fig. 2, there is an unphysical space mapped by the coldest and lowest spectral index in the hot dust
 708 grid. This corresponds to large over-subtraction and negative areas in the cold dust amplitudes as can be seen in Fig. D.3. Similar

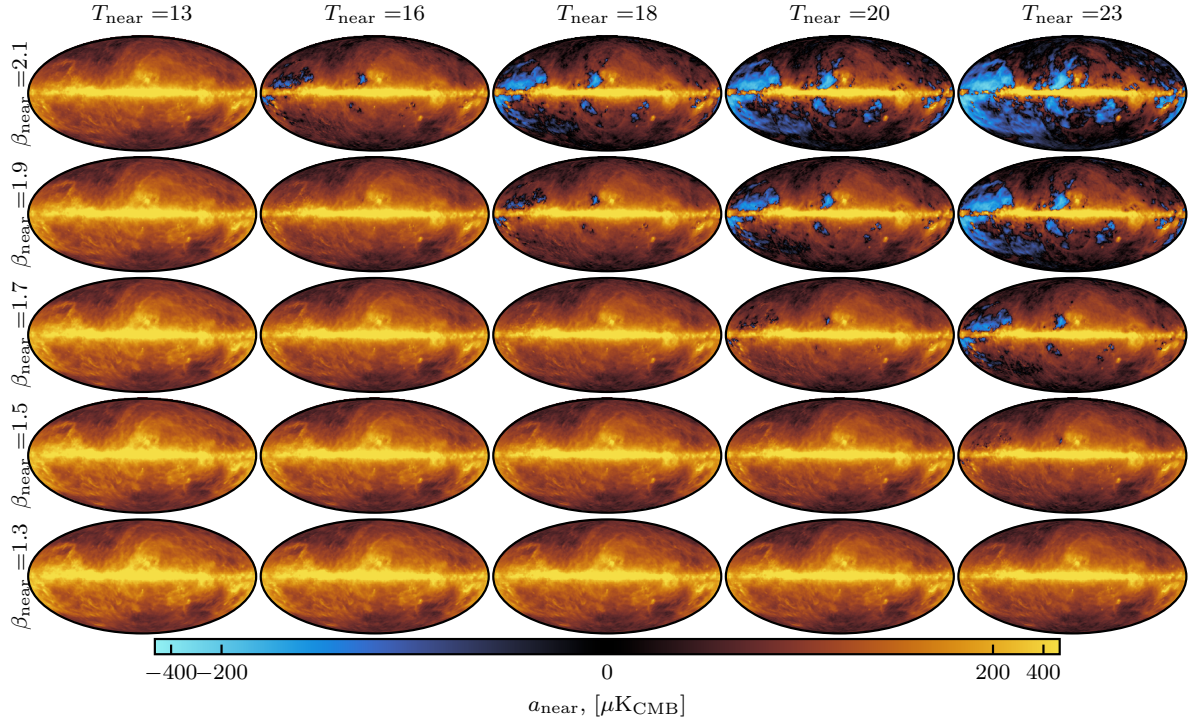


Fig. D.5: Hot dust amplitudes for varying T_{near} and β_{near} values with all other grid parameters set to the fiducial values as recorded in Table 1. The center panel is the fiducial map. The corresponding cold dust maps can be seen in Fig. D.6.

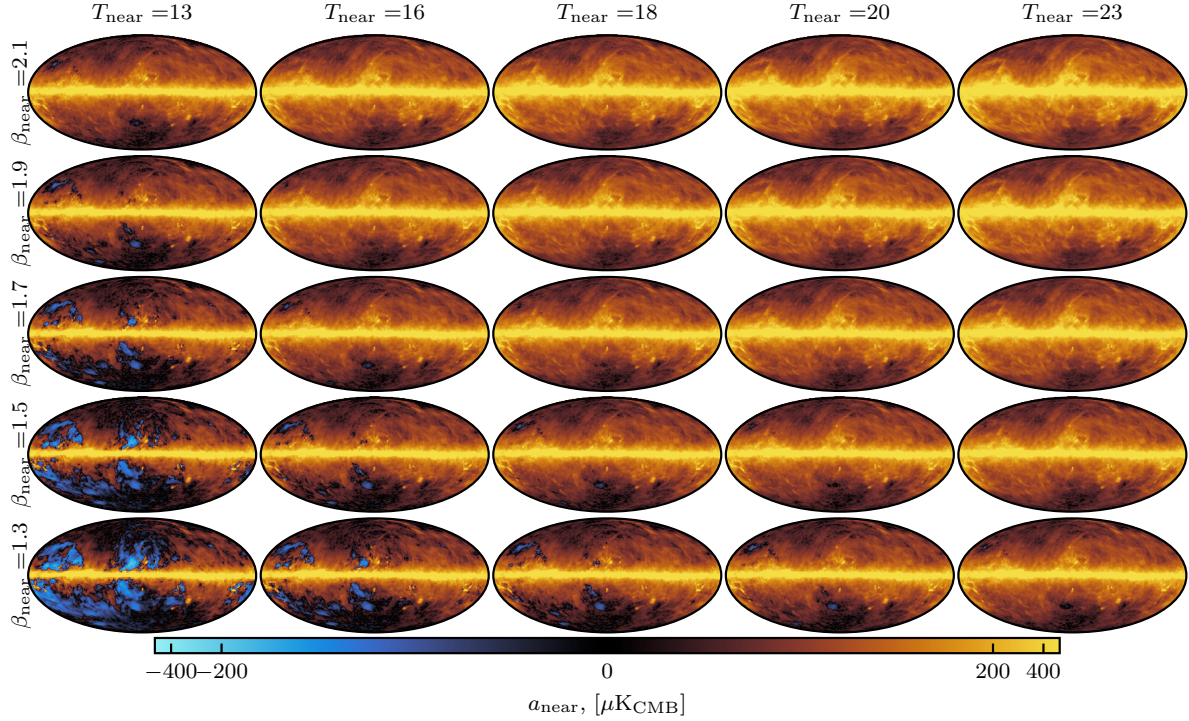


Fig. D.6: Cold dust amplitudes for varying T_{near} and β_{near} values with all other grid parameters set to the fiducial values as recorded in Table 1. The central panel is the fiducial map. The corresponding hot dust maps can be seen in Fig. D.5.

to the cold dust, when shifting the T_h and β_h we find the shape of the amplitude maps is visually similar to the fiducial map (see Fig. 4), so we show the monopole subtracted ratio of the grid position to the fiducial value in Fig. D.4. 709
710

Appendix D.3: Nearby Dust

The nearby dust was found to have unphysical regions banded both by the cold dust amplitudes and the hot dust amplitudes. We 711
712 additionally aimed to minimize correlations between the cold and nearby, and hot and nearby, dust, such that the dust population 713

714 described by the nearby dust was an independent dust component. For regions with lower β_{near} and lower T_{near} the cold dust starts to
 715 behave unphysically and this corresponds also to a higher correlation between the nearby dust and the hot dust (visible in the lower
 716 left panels of Fig. D.5). Conversely, for regions with higher β_{near} and higher T_{near} the hot dust starts to behave unphysically and this
 717 corresponds also to a higher correlation between the nearby dust and the cold dust (as can be seen by eye in the upper right panels
 718 of Fig. D.6).

719 Appendix D.4: $H\alpha$ dust

720 The parameter space explored for the $H\alpha$ correlated dust was shown to have a very flat χ^2 profile, and minimal changes to the hot
 721 and cold dust amplitudes and correlations. Since there is no perceivable difference, then, in the cold and hot dust amplitudes during
 722 the grid search, we do not include those plots here. As a reminder, we chose to take the DIRBE fit values from Gjerløw et al. (2026a)
 723 for our fiducial values since the HFI have so little control of this dust component and as we expect the DIRBE bands to have better
 724 control of these SED parameters.

725 Appendix E: Thermal dust map characterization

726 We compare the fraction of each dust component contributing to the total in Fig. E.1. As the $H\alpha$ dust is a dust extinction, with
 727 negative amplitude, it contributes a negative fraction, and it is the smallest contributor to the total. The nearby dust dominates
 728 outside the plane of the galaxy (which is to be expected, since further dust will be closer to the Galactic plane due to geometry). The
 729 hot dust is clustered nearby the galactic center and shows some anti-correlation with the $H\alpha$ dust. Finally, the cold dust is dominant
 730 in the Galactic plane further from the Galactic center. This further cements the notion that this updated dust model is more physical
 motivated than previous models, tracing known physical regions within the Milky Way Galaxy.

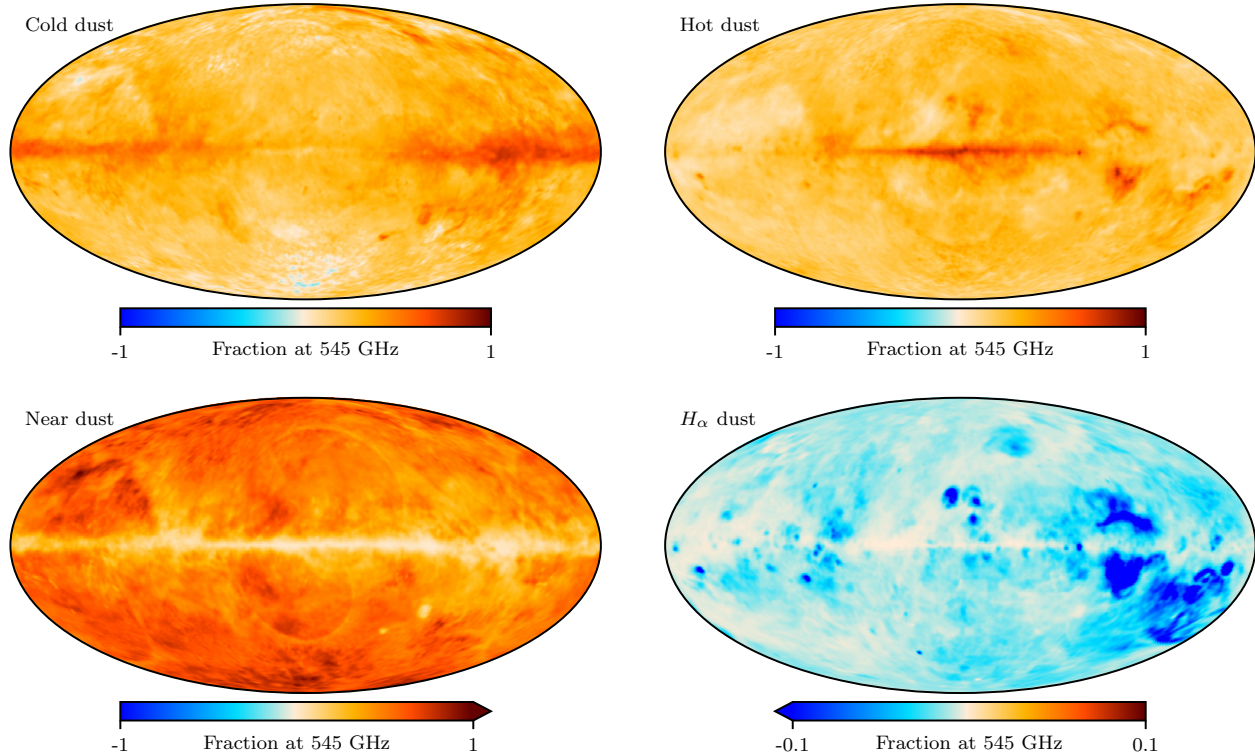


Fig. E.1: Average dust from each component contributing to the total dust signal.